MEMRISTIVE PROPERTIES OF THIN FILM CUPROUS OXIDE

THESIS

Brett C. Castle, Captain, USAF

AFIT/GMS/ENP/11-M01

DEPARTMENT OF THE AIR FORCE
AIR UNIVERSITY

AIR FORCE INSTITUTE OF TECHNOLOGY

Wright-Patterson Air Force Base, Ohio

AFIT/GMS/ENP/11-M01

MEMRISTIVE PROPERTIES OF THIN FILM CUPROUS OXIDE

THESIS

Presented to the Faculty

Department of Engineering Physics

Graduate School of Engineering and Management

Air Force Institute of Technology

Air University

Air Education and Training Command

In Partial Fulfillment of the Requirements for the

Degree of Master of Science in Materials Science

Brett C. Castle, BS

Captain, USAF

March 2011

MEMRISTIVE PROPERTIES OF THIN FILM CUPROUS OXIDE

Brett C. Castle, BS

Captain, USAF

Approved:

_____   _____
Alex G. Li, PhD (Chairman)   Date

_____   _____
Robert L. Hengehold, PhD (Member)   Date

_____   _____
Ronald A. Coutu, Jr., PhD (Member)   Date

_____   _____
Joseph E. Van Nostrand, PhD (Member)   Date

Abstract

Memristive properties of thin film copper oxides with different grain sizes were characterized using tunneling atomic force microscopy (TUNA) and optical reflection measurements. The thin films containing copper ions of different chemical states were prepared by thermal oxidation of metallic copper thin films, deposited via magnetron sputtering onto silicon wafer substrates at an elevated temperature for various lengths of time. The TUNA measurements showed a memristive hysteresis in the I-V curves under an applied bias profile with an initial bias of -3.5V, a ramp up to 3.5V, and subsequent return to -3.5V. Histogram analysis of the barrier height distribution for the forward and backward bias indicated that the barrier height fluctuates in a narrow range of bias voltages that are related to electrochemical potentials for oxidation/reduction of copper ions. Changes in chemical state of copper atoms were identified by optical reflectance measurements in UV-VIS-NIR wavelength regions. The growth of the thin films, including grain size, were characterized by topographic AFM imaging and changes in optical absorption bands due to the quantum size confinement effects. The fluctuations in the I-V measurements are theorized to be results of electrochemical changes as mobile ions migrate along grain boundaries due to heterogeneities in grain orientation/structure. A subtle periodic behavior and the variability of the I-V data suggest a correlation with grain size distribution. The asymmetric distribution in the barrier height may indicate that a different probability for injecting an electron in and withdrawing an electron from the films.

Acknowledgments

I would like to thank my wife for her love and support during this endeavor. I would also like to express my sincere appreciation to my committee chair, Dr. Alex Li, for his guidance throughout the project and to the other members of my committee, Dr. Robert Hengehold, Dr. Ron Coutu, and Dr. Joseph Van Nostrand for their active involvement during various stages of my work. Thanks are also due to my academic advisor Dr. Larry Burggraf for the direction he provided.

Brett C. Castle

Table of Contents

List of Figures

MEMRISTIVE PROPERTIES OF THIN FILM CUPROUS OXIDE

I.   Introduction

Electronic switches, namely solid state transistors, have revolutionized the world by providing us with cheap and fast methods of data processing. However, transistors as they are currently designed are approaching some physical and theoretical limits of size. As the transistor has approached the nanometer regime it has encountered problems due to quantum effects specifically increases in quantum tunneling [1]. To continue the trend of increasing data processing power per area, many efforts are ongoing to develop different methods of data processing and various designs of new electronic switches.

Another area of concern with current solid state transistors is their volatile nature, namely they require power to maintain their state of memory. Indeed there have been many methods to develop non-volatile memory, and while many of these methods have proven successful they seem to have drawbacks such as cost, size, or performance. The concept of a memristor may be the answer to both issues of size and non-volatile memory.

Leon Chua first developed the concept of the memristor in the 1970s. The three fundamental two-terminal elements in circuits, namely resistors, conductors, and inductors demonstrate the relationship of two of the four principle characteristics of a circuit—voltage, current, flux, and charge. However, these elements cannot relate flux to charge. Leon Chua identified the incompleteness of the electric circuit theory and

described a fourth element that would relate charge to flux. He identified this element as a memristor [2].

The memristor, with memristance M, defines the rate of change of flux with charge [2][3][4]. The theory has been used to describe many different systems theoretically but a fundamental circuit element had proven difficult to realize due to the focus on flux and charge [4]. It wasn't until the connection was made that a memristor also was typified by the nonlinear relationship between current and voltage that progress was made on fabricating a device [4]. This relationship is typified by a hysteresis loop on the I-V curve and also by the relationship of current to the change in voltage. Such a current-voltage relationship is typical of the bipolar-resistive switching phenomena which has been observed and studied since the 1960s [5][6] and is the mechanism used today in resistive random-access memory (RRAM).

Bipolar-resistive switching is a phenomenon that occurs when a voltage is applied over a dielectric material, solid electrolyte, transition metal-oxide, or semiconductor material. On a macroscopic scale, such a metal/insulator/metal (MIM) system describes a capacitor. The dielectric medium in the capacitor has high resistance preventing current to flow. When a significantly high voltage is applied across the medium, it irreversibly breaks down; no longer able to stop the flow of current. On a nanometer scale, applying even a small voltage across such a short distance creates an enormous electric field. Such a field not only causes the flow of electrons but also causes ions to move within the medium [1][7]. This ion movement causes a change in the resistive state of the medium. Furthermore, by reversing the polarity of the applied voltage the medium can return to its

original resistance, hence demonstrating the features of an electric switch. The resulting I-V curve is due to the coupling of electronic and ionic mobilities and can be best described as a memristive relationship [1]. Many times researchers dismissed this phenomenon as "anomalous" or due to "spurious phenomenon attributed to the high voltages", but it is apparent now that memristance becomes more prevalent as the medium approaches the nanometer scale and even becomes the dominant relationship [8]. Memristance is therefore ideally suited for the nanometer regime of electronics.

Within the last decade there has been additional studies trying to identify the mechanism(s) involved with bipolar-resistive switching. Strukov *et al* describes the mechanism as a shift in the dividing line between two states of a transition metal oxide [4]. As oxygen vacancies migrate from a conducting oxygen-deficient layer into an insulating stoichiometric layer it changes the resistance of that layer. The vacancy movement continues until a minimal resistive state is reached at which point the polarity of the applied voltage can be reversed sending the oxygen vacancies back into the oxygen-deficient layer.

Other evidence supports a different approach describing the dominant process taking place as the growth of microfilaments through the medium connecting the two electrodes [1]. Prior to any filament growth the medium is in a high-resistance state. After applying a relatively high "forming" voltage, the medium experiences a "soft" dielectric breakdown in a region between the two electrodes [9]. This region experiences a change in valence and typically is along a defect [1]. Within this region a filament grows connecting the two electrodes. Once the medium has gone through the forming process it

3

changes to a low-resistance state. This binary switch remains in this low-resistance state until a RESET voltage of opposite polarity is applied hence demonstrating a non-volatile characteristic. This change in polarity causes the ions to migrate through the medium in the opposite direction returning it to its high-resistance state. After the forming process, the medium can be cycled through the two resistive states by applying a SET voltage that is lower than the forming voltage and a RESET voltage [1]. The process is reversible and has been shown to occur along the same path of prior filament growth [1].

Explanations have been given for filament growth in the MIM system, but not all systems or materials support the theory and other explanations are used to describe the resistive switch mechanism. Ion hopping is thought to be the dominant mechanism leading to filament growth. Charged ions begin to build up at the electrode thus creating a cation filament and/or region of reduced valence. This build-up continues until a connection between the electrodes is made. This process tends to take place along dislocations, defects, or boundaries where movement is more conducive due to lower activation energies [1]. One question is what part joule heating plays in the filament growth. There is a possibility the flow of electrons could heat the path to the point of reducing the region and causing the oxygen ions to vacate [1]. Studies have also been done to determine the effect electrode area plays in the observed current raising questions as to whether multi-filaments and multiple paths are possible [1].

Another theory that has been used to describe the I-V behavior of the resistive switches is space-charge-limited-current (SCLC) theory [10]. SCLC describes the injection of carriers from an ohmic contact into a thin film insulator or semiconductor.

The I-V relationship is characterized first by a linear region of high resistance, followed by a region where the relationship is described by Child's Law (current is proportional to V^2), and lastly another linear region beginning at the trap-filled-limit voltage (V_{TFL}) with a steep increase in current. The theory describes this behavior to be dictated by traps within the bandgap that are filled by the injection of carriers from the ohmic contact. The measured current in turn is influenced as these traps are filled and the Fermi energy level changes. It appears as though this theory focused on micron thick films when first developed and not nanometer thick films which opens further questions as to the influence the high electric fields will impact the behavior of the charge carriers within the film.

In 2008 Strukov *et al* reported successful design of a memristor device [4]. The device used depleted TiO_2 as the dielectric medium in a crosshatch design. A thin wire of conducting titanium, serving as one electrode, is layered with a thin film of insulating TiO_2 and another thin film of TiO_{2-x} which is a good conductor due to the oxygen vacancies donating electrons. The other electrode is formed by laying thin conducting wires of Pt across the top of the TiO_2 film thus completing the MIM structure. In this system, oxygen vacancies act as mobile charged dopants, which drift in the applied electric field. As they drift they shift the dividing line between the TiO_2 and TiO_{2-x} layers and consequently change the resistance. The crosshatch design is thought to be the optimal configuration for bits per area and work is already being done to incorporate such a device into circuits [8].

This system has proven to perform well because TiO_2 serves as a good medium due to the high mobility of oxygen vacancies within the lattice and the high conductivity of TiO_{2-x}. Another material that seems promising is Cu_2O because Cu^+ has high mobility and should drift well through the Cu_2O lattice. Copper is also inexpensive, a current staple of electronics, and is non-hazardous. Work has already been done demonstrating the memristive properties of copper making it ideal for further study [11].

1.   Problem Statement

Electronics are increasingly becoming smaller and faster. Theory and evidence shows the memristor to be a possible answer to the problems encountered when designing electronics at the nanometer scale. Experiment has demonstrated memristors can be made via the bipolar resistive switching phenomenon found in transition metal-oxides. The transition metal-oxide Cu_2O has properties favorable for the electronics industry and may prove an excellent material as a memristor device. It is the focus of this effort to add further knowledge to the memristive properties of Cu_2O and its possible application as a memristor device using atomic force microscopy (e.g., TUNA module).

2.   Research Objective

The objective of this current effort is to characterize the electronic properties of thin film Cu_2O using the AFM. This effort will aim at correlating the oxidation state of the Cu_2O film with the observed I-V relationship and draw conclusions to the process taking place leading to the non-linear relationship. The oxidation state will be characterized using visible spectroscopy and the I-V relationship will be measured via TUNA.

There are many interesting aspects of this phenomenon that could be studied in greater detail such as forming voltage, SET voltage, RESET voltage, switching speed, Cu^+ mobility, effects of thickness and oxygen concentration, effects of electrode size, effects of boundary and plane orientation, filament growth, and the change in valence boundary/oxidation state due to applied voltages. Another area of interest is the contribution of Joule heating to filament growth. It may be possible to measure the heat created from the flow of electrons between to lateral electrodes using the AFM with a thermal module. There have also been studies showing the impact of dopants to the mechanism. One study describes the dopants as islands which connect the filament as it grows from island to island. It is thought that such dopants could increase switching speeds. Another concern may be the effects of temperature or radiation on resistivity. Many applications require electronics to operate in either extremely cold or extremely hot conditions or be radiation hardened. The various temperatures may affect switching speeds or the measured resistance. An extreme change in temperature or radiation may switch the state of the device.

Other aspects that could be studied are the effects of annealing, oxide growth methods (i.e. thermally grown oxide, chemically oxidized, vs. sputtered copper-oxide), and electrode material. Annealing can affect the carrier mobility and may alter the memristance of the material. Rakhshani reported changes in electrical properties of electrodeposited films versus cuprous oxide films thermally grown on bulk copper [12]. The material of the electrode may also play a role in memristance due to the change in space charge regions or hole/electron carriers.

3.   Research Impact

Memristors could provide ultra dense memory at remarkable speeds. In addition, they provide a viable and cost-efficient answer to non-volatile memory; furthermore they prove to be well-suited to function as an EMP hardened form of memory. Companies are currently designing electronics to incorporate memristors [8]. Some materials may even have continuous-resistive states or multiple resistive states opposed to bi-resistive states which could ultimately lead to analog memory as found in the neurons of the brain. Cu_2O might demonstrate properties well-suited for use as a memristor. AFM techniques developed and used in this effort may also show promise for future studies of memristive materials.

4.   Methodology

This effort will consist of sample preparation and various methods of characterization. The samples will be prepared to create a metal-insulator-metal system on nearly atomically flat doped-silicon wafers of <111> plane orientation. The samples will then be cut into smaller samples and oxidized at varying times in order to create varying states of oxidation on the surface. Reflectance data of the samples will be collected and used in order to estimate the oxidation state. AFM data will also be collected in order to characterize surface features and estimate how this data may impact other measurements. The TUNA will be used to ramp from a negative voltage to a positive voltage and then back to negative at stagnant locations in order to collect I-V data on the sample. The collected data will then be used in order to draw conclusions as to the process taking place at the surface of the sample.
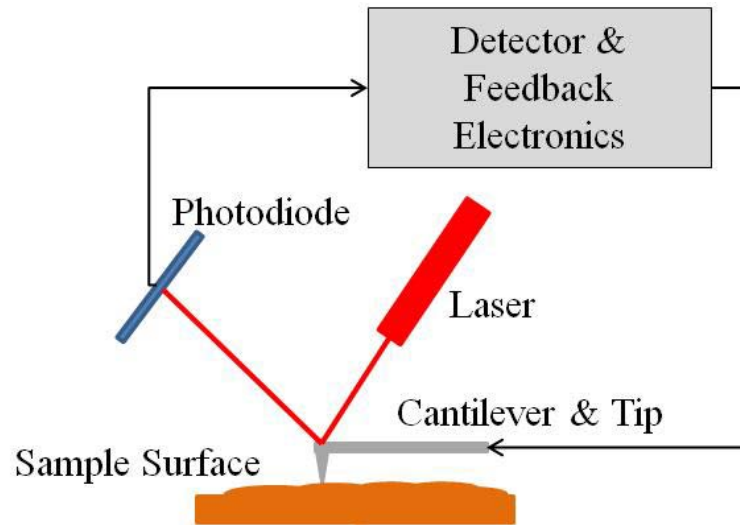
Figure 1. Schematic of the Atomic Force Microscope (AFM). A cantilever applies a small force on the surface of a sample via a nanometer sharp tip. The deflections from the surface are relayed back to the detector via deflections from the laser reflection off the backside of the cantilever and changes in the force sensed by the piezo electric crystal.

The AFM is a powerful tool for studying nanotechnology. The AFM drags a nanometer sharp tip across the surface of a material. As the tip moves across the surface it is deflected by the surface features of the material. The AFM uses a laser to measure the deflection of the tip by the surface thus providing an image of the surface. The AFM is able to get nanometer resolution of surface features making it ideal for the study of materials in the nanometer regime. By using a conductive tip and applying a voltage across the sample and the tip, the AFM is also able to measure currents and tunneling currents. The tunneling AFM (TUNA) measures tunneling currents across thin insulating films which is well-suited for the study of bipolar resistive switching in oxide films.
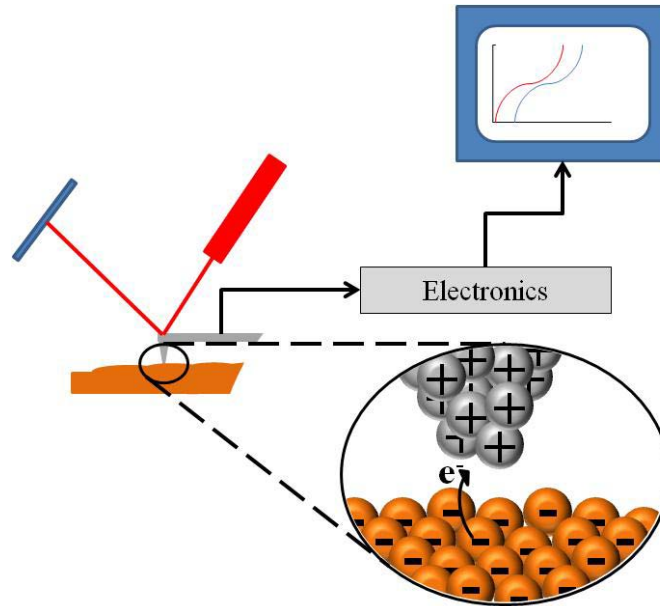
Figure 2. **Schematic of the principles of Scanning Tunneling Microscopy (STM) and Tunneling Atomic Force Microscopy (TUNA). Much like the AFM, TUNA drags a tip across the surface and collects surface data. TUNA and STM, however, apply a voltage across the sample from the sample mount to the probe tip. This voltage results in a tunneling current that is read by the sensors and provides electronic property profiles.**

Diffuse reflectance spectroscopy probes the surface of the sample with light of varying wavelengths. This light will be affected by many factors including band structure, surface roughness, and sample thickness. Cuprous oxide has a bandgap of 2.1eV (591nm) and cupric oxide has a bandgap of 1.2eV (1034nm) which absorbs light at those energies/wavelengths which would result in a minimum in reflectance. As thickness layers approach the size of the wavelength of the incident light (hundreds of nm to a few microns) the reflected light can encounter constructive and destructive interference leading to oscillations in the reflected light's intensity with varying wavelength. The thermally grown oxide has varying characteristics in bandgap, thickness, surface roughness, and other characteristics which the reflectance data should be able to highlight.

II.   Sample Production and Characterization

1.   Sample Production

The samples are designed to create a MIM system using copper as an electrode, copper oxide as the insulator, and the platinum/iridium doped silicon AFM tip as the other electrode (shown in Figure 3). In order to prevent oxidation on the copper electrode a gold electrode was placed on the copper. The wafer with the deposited metals is cut into smaller samples for testing. The copper oxide is thermally grown by oxidizing the exposed copper samples in a quartz tube furnace in a 50/50 mixture of oxygen and argon gas flowing over the surface at 20 psi.
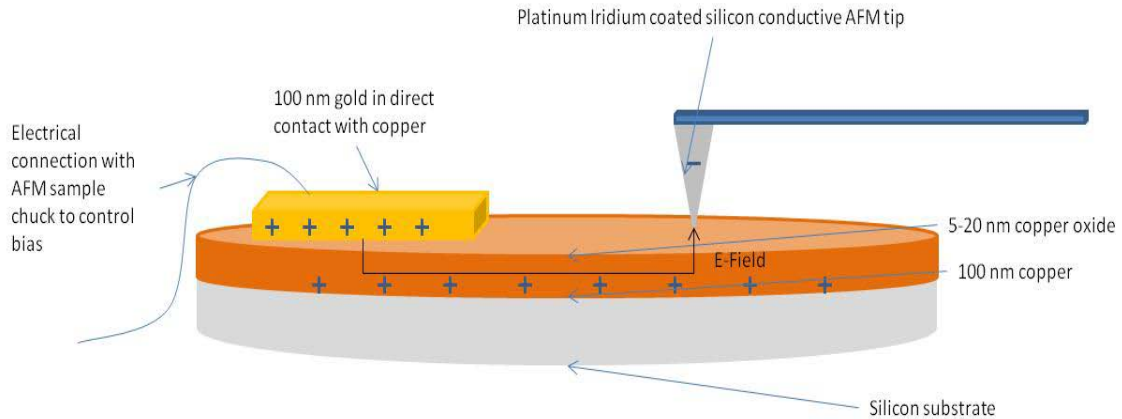
Figure 3. Schematic of sample highlighting MIM structure with AFM tip as an electrode.

Two <111> silicon wafers were cleaned using methanol, acetone, isopropyl, distilled water, nitrogen gas, and heated on a hot plate for approximately 60 seconds at 100 °C. Thin layers of copper roughly 100 nm in thickness were deposited on the wafers using a Denton 18 plasma deposition system in an argon atmosphere at a pressure of 3.7mTorr. Sputter deposition is a form of physical vapor deposition (PVD) in which a target is

11

bombarded with ions causing particles on the target to be ejected and subsequently be deposited on a substrate or sample. The method used in this effort was to create argon plasma which is controlled by the magnetic fields of a magnetron. The magnetron directs the argon ions to impact the copper target which ejects copper atoms onto the silicon wafer. Once the copper was deposited, the wafers were removed and immediately placed in the evaporation chamber where 100 nm of gold was deposited on top of the copper through a stainless steel shadow mask (as shown in Figure 4). Evaporation deposition is another form of PVD in which the target material is heated until it boils off and is subsequently deposited on the sample. This method was used due to available resources.

The wafers were then cut using two methods. The first wafer was cut using a diamond scribe and then broken by hand. The cuts were rough and resulted in scratches on the sample surface. Gold wires were then bonded to the gold contact at 100 °C for less than 5 minutes after which the samples were oxidized in the quartz tube furnace and subsequent reflectance data measured. The second wafer was cleaned (as described above for cleaning the wafer without the application of heat) and then coated with 1818 photoresist. After the photoresist was applied the wafer was heated at 100 °C for 5 minutes in order to cure the photoresist. The wafer was then cut by a computer controlled diamond saw. Each resulting sample was then cleaned to remove the photoresist and then oxidized in the quartz tube furnace. Reflectance data was then collected on these oxidized samples after which a gold wire was bonded to the gold contact as described above.
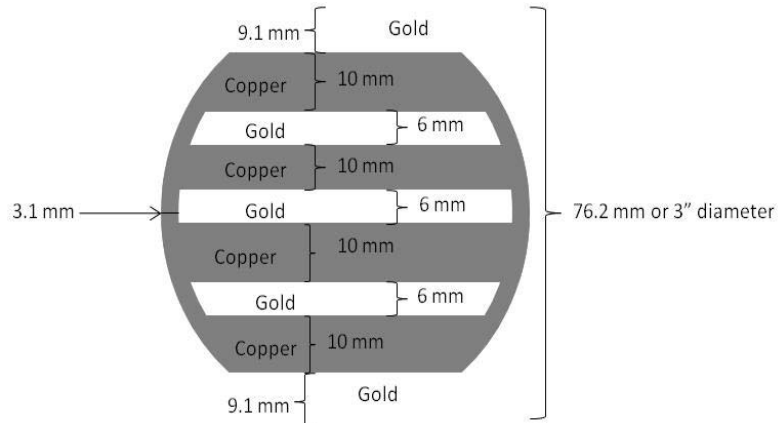
Figure 4. Mask #1 used in phase 1.

Samples were oxidized in the quartz tube furnace at 125°C under 20psi of a 50/50 oxygen/argon mixture for various lengths of time. The times were 45 seconds, 90 seconds, 135 seconds, 5 minutes, 10 minutes, 15 minutes, 30 minutes, 45 minutes, 60 minutes, and 120 minutes. Images of the noticeable color change in the oxidized samples are shown in Figure 5.
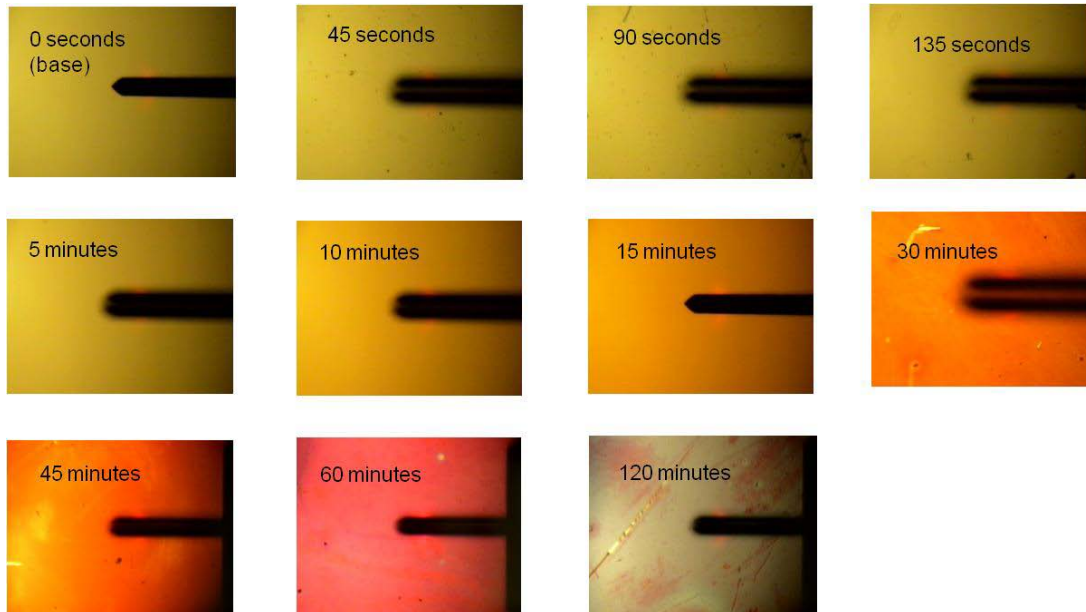
Figure 5. Surfaces images taken of the prepared samples with optical microscope

2.   Sample Characterization

The oxidized samples were characterized using diffuse reflectance spectrometry and the tunneling AFM. The diffuse reflectance spectrum provided band gap information and information regarding surface particle size. The TUNA provided surface topography and a current voltage relationship.

Reflectance data was collected on a Cary 5000 UV-Vis-NIR Spectrophotometer. Background measurements were first collected on a reference plate of inert plastic powder which the machine subtracted from the collected data. A zero reference was also collected with no sample mounted in the machine. In order to ensure the gold on the surface did not contribute to the measured data, an aperture was used to cover the samples making sure only the copper was exposed to the incoming light. Consequently, the aperture was also sampled which was later subtracted from the measured data. When collecting data, the lights in the room were extinguished in order to ensure no background light was interfering with the measurements.

A Veeco Dimension V mounted with a TUNA application module was used to collect I-V information. The AFM was mounted with a SCM-PIC platinum-iridium coated antimony doped silicon tip. The antimony doped silicon has a resistance of 0.01 - 0.025Ωcm. The tip has a nominal radius of 20nm and a max radius of 25nm and a tip height of 10-15µm. The cantilever has a nominal spring constant of 0.2N/m with a minimum at 0.1N/m and a maximum of 0.4N/m. The samples were mounted on Scotch double-sided tape and then attached to a glass slide with the copper facing up. This ensured the sample was fully insulated and no current would pass through the silicon

wafer substrate. The AFM sample chuck was electrically connected to the copper electrode (via the gold wire on the gold surface electrode) on the sample thus producing a metal (copper)/insulator (copper oxide)/metal (platinum iridium coated AFM tip) structure. A force plot was done on each sample before I-V measurements were conducted. The deflection setpoint was adjusted to ensure a constant 10nN of force was applied on each sample. Two sets of I-V data were collected. The first set of data was conducted at -3.5V to 3.5V continuous ramp at 0.25Hz, 10pA/V current sensitivity, for 76 captures. This was repeated at 5 locations in the XY coordinates at (0, 0), (-250nm, 250nm), (-250nm, -250nm), (250nm, 250nm), and (250nm, -250nm). The second set of data was collected at -3.5V to 3.5V continuous ramp at 0.25Hz, 100nA/V current sensitivity (the least sensitive setting), for 24 captures. This was repeated at 5 locations in the XY coordinates at (0, 0), (250nm, 0), (250nm, 250nm), (250nm, -250nm), and (-250nm, -250nm).

The contact area between the tip and the surface can be modeled to a first approximation by the contact of an elastic sphere with a flat elastic surface. Using this model the area can be estimated using equations (1)-(2) where R_c is the contact radius, r is the curvature radius of the tip (estimated at 20nm), F is the applied force (10nN), E is the effective Young's modulus, E_1 is the Young's modulus of the surface (estimated using the value of copper, $1.31 \times 10^{11} N/m^2$), E_2 is the Young's modulus of the tip (estimated using the value of silicon, $1.69 \times 10^{11} N/m^2$), υ_1 is Poisson's ratio of the surface (estimated using the value of copper, 0.351), and υ_2 is Poisson's ratio of the tip (estimated

using the value of silicon, 0.278) [13]. This results in an estimated contact radius of 1.22nm and a subsequent contact area of 4.69nm^2.

$$R_c = \left(\frac{3rF}{4E}\right)^{1/3} \tag{1}$$

$$E = \frac{1-\upsilon_1^2}{E_1} + \frac{1-\upsilon_2^2}{E_2} \tag{2}$$

The force applied on the surface and the resulting contact area is relatively small. Elastic deformation is expected although plastic deformation of the surface would be doubtful. With such a small applied force the probability of piercing the oxide layer and making contact with the copper electrode is small. Electrostatic deflection due to the applied bias between surface and tip is expected, although deflection measurements taken concurrently with current measurements showed no indication of deflection. Similar tests were conducted after this experiment where deflection was measured but current was not. Force plots taken with the AFM indicate the existences of adhesive effects due to Van der Waal's forces. This force is relatively small (~1nN) as the tip approaches the surface and greater when the tip retracts from the surface (~6-10nN).

The surface images were collected by the AFM in tapping mode using a silicon tip. The tip was auto-tuned to ~74kHz before each image. The integral gain and proportional gain were in general set to 0.5V and 1V respectively; minor adjustments were made to improve image quality if needed. Scan settings were 0° scan angle, 1µm scan size, 512 lines/sample, 512 lines, and in general 0.5Hz scan rate.

III.   Results and Analysis

1.   Reflectance Results

Figure 6 shows the base data subtracted from the reflectance data from 200 to 800nm. The absorption peaks can be more easily seen by subtracting this data from 100 as illustrated in Figure 6. Noticeable peaks can be seen in the range of 650nm, 600nm, 470nm, and 200nm. Smaller peaks can also be seen in the range of 330nm and 250nm. It is quite evident the wavelength of the peaks and their relative intensities changes with respect to oxidation time. (See Appendix A Reflectance Results for further reflectance data).
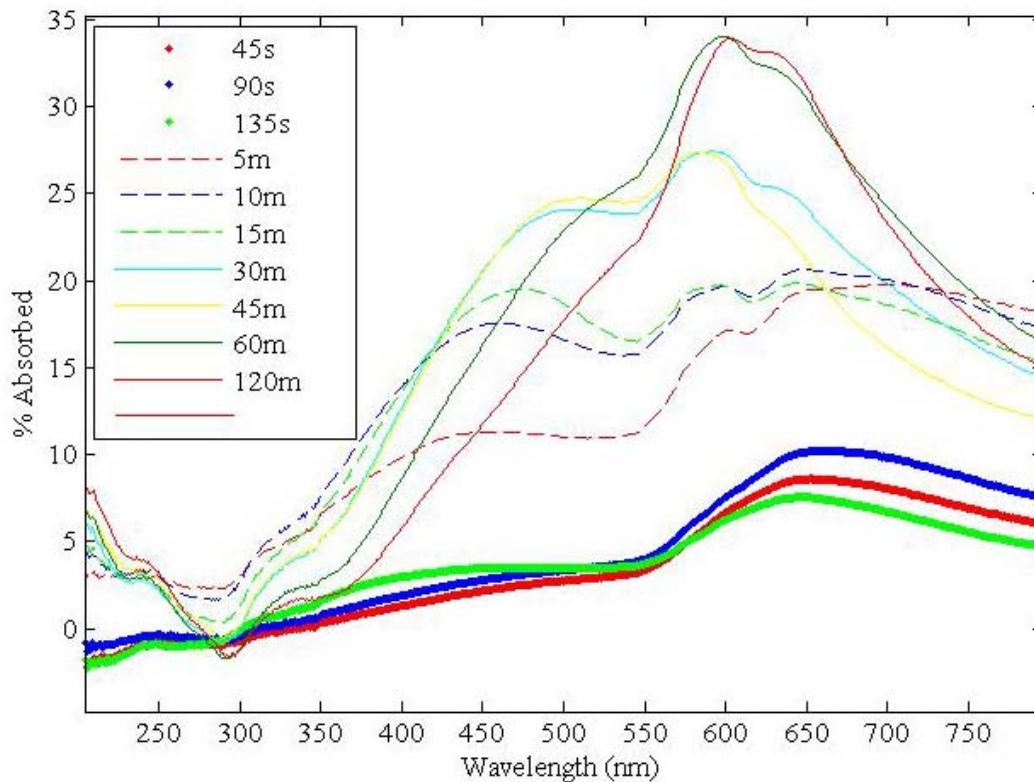

Figure 6. Absorption vs wavelength

Most of the observed structures and trends can be collaborated with reported results. Copper has been reported to have absorption structures at 300nm and 550nm [14] which are evident in the raw base sample spectrum (Figure 20). Features near 650nm in the low-oxidation samples may be due to the optical properties of bulk copper. The reported value for the band gap of bulk Cu_2O is about 2.1eV or 591nm [15] which would explain the peaks around 600nm. The band gap of bulk cupric oxide (CuO) is around 1.2eV or 1034nm [15]; no noticeable features were seen in that range.

The peaks around 470nm and 330nm have also been reported to be the result of the synthesis of Cu_2O nanocrystals of varying sizes resulting in quantum effects [16]. Deki *et al* reported a broad absorption shoulder at 350nm for 6.7nm sized particles [17]. Knözinger *et al* reported a broad feature at about 450nm for Cu_2O nanoparticles having an average particle size of 9nm [18]. Banerjee *et al* reported the energy peak of one feature increased from 2.25eV (551nm) to 2.6eV (477nm) with a decrease in particle size from 8.6 to 4.8nm and another peak shifted from 1.77eV (700nm) to 2.37eV (523nm) corresponding with a decrease in particle size from 8.6nm to 6nm [19]. From these reports, the additional peaks in the collected data could be explained by the quantum confinement effects from the growth of Cu_2O nanocrystals on the surface of the copper.

Absorption spectrum observed in semiconducting materials is best described by band theory. Atoms or molecules have distinct electronic energy levels as described by quantum mechanics theory. As atoms are brought together by Van der Waal's forces and form into crystalline structures, these energy levels split due to the interactions from neighboring atoms. As more atoms form the crystal the energy-level splitting continues

until the energy levels become nearly continuous and energy bands are formed (see Figure 7). Such energy bands describe the properties of bulk semiconducting materials. Electrons in the conduction band can absorb incoming photons and transition to the valence band as long as the energy of the incoming photon is greater than the bandgap or minimal distance between the highest point in the conduction band and the lowest point in the valence band. This results in a broad absorption spectrum.
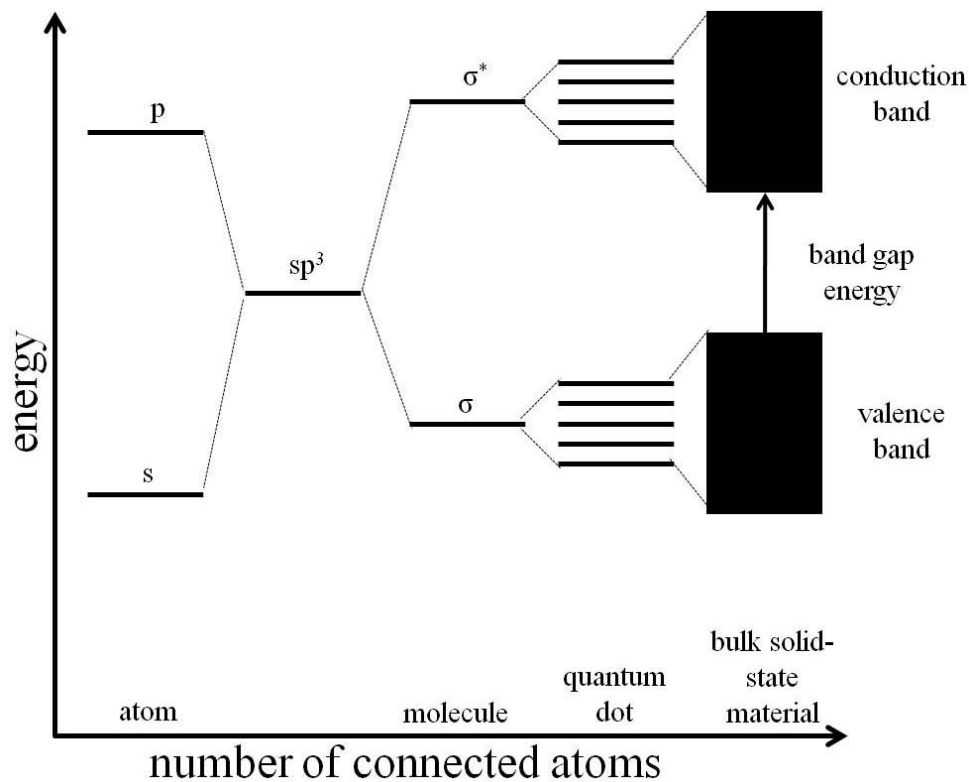
Figure 7. Electronic energy levels depending on the number of bound atoms. By binding more and more atoms together, the discrete energy levels of the atomic orbitals merge into energy bands (shown here for semiconducting material). Semiconducting nanocrystals (quantum dots) can be regarded as a hybrid between small molecules and bulk material.

Quantum confinement is a phenomenon that occurs when semiconducting materials are confined in at least one of the three spatial dimensions by nanometer lengths. When

19

the material is confined in all three dimensions the material is called a quantum dot. The number of atoms in a quantum dot is such that energy level splitting occurs, but not to the extent that banding occurs. Typically the resulting energy levels cause the minimal energy required for electron excitation to increase resulting in a blue shift in the absorption spectrum (see Figure 8).
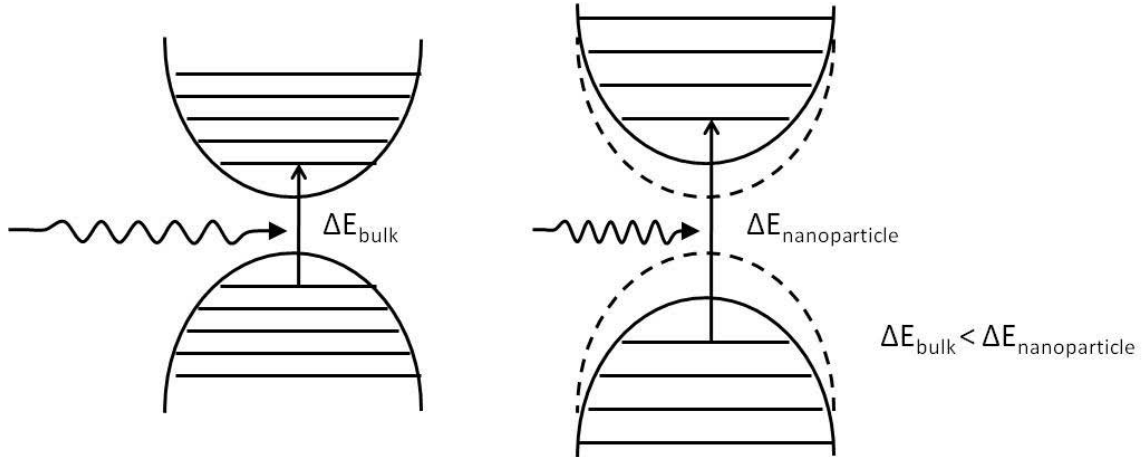
Figure 8. Schematic of quantum confinement effects of nanoparticles on bulk band structure.

This shift in the spectrum can be calculated from equations (3)-(6) [20]. E_{well} describes the energy of the potential well created by the quantum dot where m^* is the effective mass of the electron.

$$E_{well} = \frac{\hbar^2}{2m^*d^2} \tag{3}$$

E_{Coul} is the Coulomb attraction of the exciton which also contributes to the shift in absorbed energy.

$$E_{Coul} = \frac{-1.8e^2}{2\pi\varepsilon\varepsilon_0 d} \tag{4}$$

20

$E_{g,dot}$ is the resulting expected energy shift in absorption. Inserting equations (3) and (4) into (5) results in equation (6).

$$E_{g,dot} = E_{g,bulk} + E_{well} + E_{Coul} \tag{5}$$

$$E_{g,dot} = E_{g,bulk} + \frac{\hbar^2}{2m^*d^2} - \frac{1.8e^2}{2\pi\varepsilon\varepsilon_0 d} \tag{6}$$

A first order estimate of the diameter of the nanoparticle can be derived from the energy of the potential well. Estimating the effective mass of the electron to be the reduced mass of an electron with mass $0.99m_e$ and a hole with mass $0.69m_e$ and setting the energy of the potential well equal to the difference in energy from the bandgap (2.1eV) and the first observed peak (~2.6eV), results in a diameter of roughly 2.72nm. Peaks at higher energies would indicate particles with diameters down to ~1nm (6eV peak). The absence of peaks between 2.1 and 2.6eV might suggest particles in the range of 2.72nm have the optimal energetic configuration for surface tension to volume ratio. The 2.6eV peak decays in relative intensity with further oxidation after 15 minutes which may indicate the particles are getting too close together and the band structure begins to mimic bulk properties. Peaks in the higher energy range (>3.5eV) grow in relative intensity with higher oxidation. This may be indicative of 1nm sized particles, but presumably of different stoichiometry than the 2.6eV particles due to their propensity to grow at higher oxidation times.

There are relatively few features in the low-oxidized samples (45 seconds to 135 seconds) suggesting the reflectance features are dominated by bulk copper with a growing peak in absorption due to the onset of small oxidation films. The mid-oxidized

samples (5 minutes to 45 minutes) show increased number of features at various peak energies suggesting this distribution in various sized nanocrystals. As the samples are oxidized further to 120 minutes, those multiple distinct features disappear suggesting the material is behaving closer to its bulk properties. This assertion of growing surface features is supported by the AFM scans below.

CuO is known to grow in conjunction with Cu_2O in varying concentrations. These inhomogeneous growths could alter the band structure in small regions consequently affecting the reflectance data. Another observed effect on reflectance spectrum is the influence of film thickness. When oxide thickness is on the order of the wavelength of light, destructive and constructive interference could play a role in creating oscillating peaks and valleys. The oxide thickness is at a maximum 100nm (thickness of the deposited copper) and therefore does not exhibit that behavior. The oxide thickness, however, could contribute to the relative magnitude of the peaks as the number of absorbers increases with material thickness hence the increase in peak intensity. The data has not been normalized, but a general trend can been seen as the oxidation time increases the absorption peaks increase which intuitively would agree with the growth of the oxide layer.

2.   AFM Scanning Results

The AFM scan results show a trend in grain/particle size increasing after 15 minutes of oxidation. From the 30 minute oxidation to the 120 minute oxidation the contrast in peaks (bright yellow) and valleys (dark regions) becomes more evident. Furthermore, it appears as though the width of the peaks increases while the number of valleys decreases.

This would suggest the particles are increasing in both height and width. While these larger peaks and valleys are on the order of 100s of nanometers and may not play a role in the reflectance spectrum, small particles can to still be seen growing which is evidence of the overall trend.

Figure 9. AFM 1μm × 1μm scans. Note changing scales.

The Z range and R_{max} are the maximum vertical distance between the highest and lowest data points in the image following the planefit. The $SA_{difference}$ is the percent difference between the two dimensional surface area (1μ x 1μ) and the measured three dimensional surface area. The R_q is the RMS roughness or root mean square average of height deviations taken from the mean image data plane as expressed in equation (7).

$$R_q = \sqrt{\frac{\sum Z_i^2}{N}} \qquad (7)$$

R_a is the arithmetic average of the absolute values of the surface height deviations measured from the mean plane as expressed in equation (8).

$$R_a = \frac{1}{N} \sum_{j=1}^{N} |Z_j| \qquad (8)$$

From this data a trend can be seen as oxidation time increase the range in feature height increases and surface area increases indicating the growth of particles. These features may be due to various surface phenomenons such as Ostwald ripening, nucleation, or stress related features. Ostwald ripening describes the phenomenon of small surface particles in an unfavorably energetic configuration detaching and diffusing into the crystal. These particles contribute to the growth of larger surface particles. Nucleation occurs similar to Ostwald ripening where particles tend to combine in order to eliminate unfavorable energetic configurations and seek an optimal volume to surface area configuration. The longer oxidation times would also provide the necessary time and energy to allow these phenomena to occur. Copper generally forms in a face-centered-cubic structure with a lattice constant of 3.61 angstroms while cuprous oxide tends to form in body-centered-cubic structure with a lattice constant of 4.2696 angstroms. This variation in structure and lattice constant would conceivably result in surface stresses which could possibly be relieved in surface buckling or cracks as seen in the optical image of the 120min sample (Figure 5). Some surface features may also be a translation of surface features of the copper deposition.

3. TUNA Results

The TUNA data collected illustrates a the non-linearity of the I-V relationship of the cuprous oxide films. The sample chuck initially begins with an applied voltage of -3.5V and then ramps linearly to +3.5V; the measured current is recorded in the "trace" plots, typically indicated by the blue lines. The sample chuck then ramps back down to -3.5V completing the cycle. This current data from +3.5V to -3.5V is recorded as the "retrace" data. It's typical to see the current data flatline at a particular current magnitude indicating the current has saturated the measurement device. Provided are typical samples from the collected data (Figure 10 and Figure 11). Though these plots are representative of data collected, the curves fluctuated over time and varied with sample location. The curves taken of the 120 minute sample at 10pA/V sensitivity show very unique and reproducible properties (Figure 12). At distinct voltages there is a peak in current, opposite in sign to the applied bias and suggesting a negative resistance. This was only seen in the 120min sample at that sensitivity.
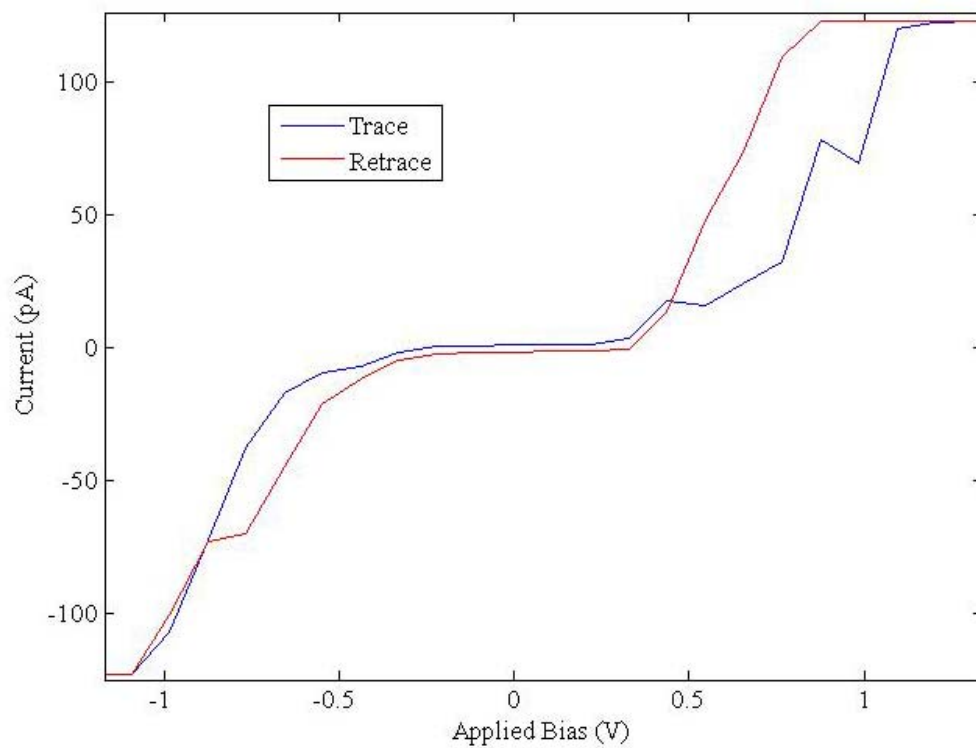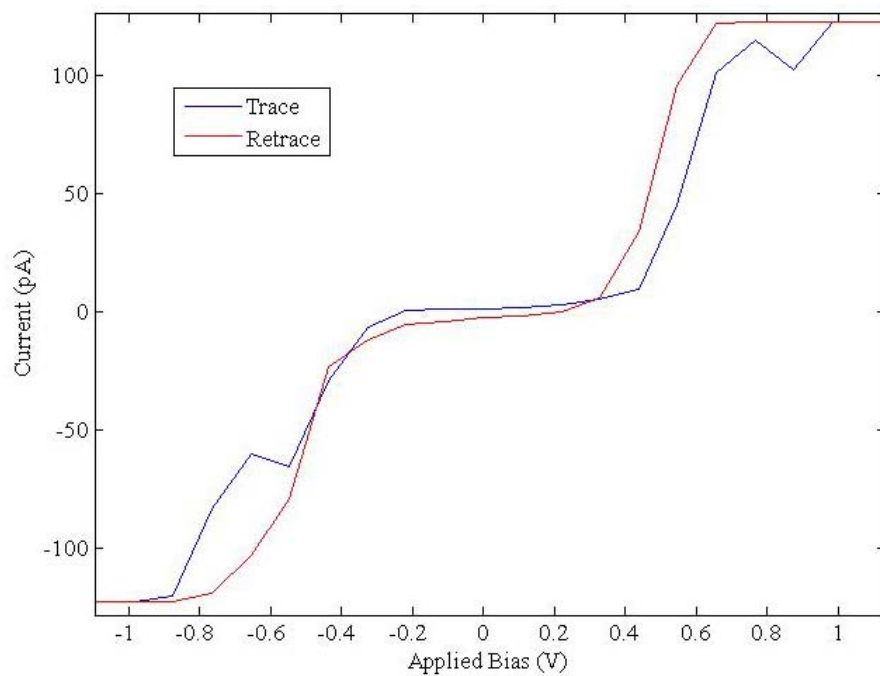
Figure 10. 5 minute sample, 10pA/V current sensitivity

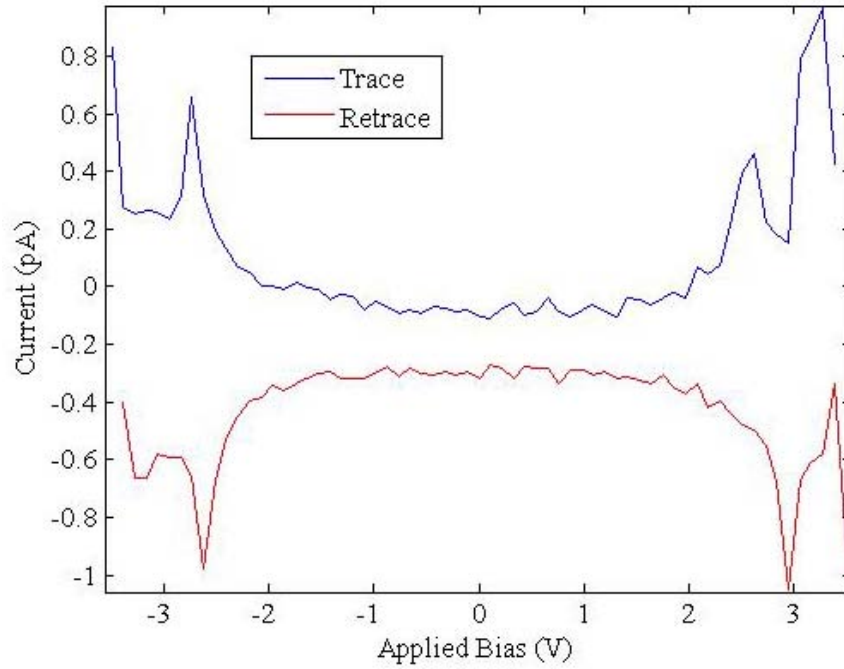**Figure 11. 60 minute sample, 10pA/V current sensitivity**

Figure 12. 120 minute sample, 10pA/V current sensitivity

The curves have distinct regions of ohmic/insulator properties, non-linear regions, and more linear regions with steep slopes. Similar current behavior has often been described by space-charge-limited-current (SCLC) theory [10]. SCLC theory attributes this behavior to the injection of free carriers into available trap states within the bandgap. At some threshold voltages the traps are filled at which point the behavior changes from linear to non-linear or vice-versa. At voltages about 0V, the voltage is too small to overcome the potential barrier created between the semiconducting material and the conducting electrode and the current behavior is ohmic/insulator like. Each curve in general follows SCLC theory with an ohmic region, a region following Child's Law (I is proportional to V^2), followed by a steep increase in current at the trap-filled-limiting voltage (V_{TFL}). SCLC theory would suggest this relationship should be reproducible from cycle to cycle within a static material. Dong *et al* reported similar results for thin

films of thermally grown cuprous oxide [11]. Their results, however, showed fairly consistent behavior and steep linear drops when ramping back from positive to negative voltages; something SCLC theory does not account for. This behavior is best described as the resistive switching mechanism from a high-resistive state to a low-resistive state and then returning to the former. Dong *et al* suggests this behavior is due to the drift of mobile Cu^+ ions through the lattice forming multi-filaments which is supported by other work. While some behavior in the results of the present effort could be described by SCLC theory, the variation in the behavior and other attributes would suggest a different mechanism is occurring within the lattice.

At times the data exhibits "diode-like" behavior and at other times exhibits a hysteresis typical of memristive behavior. While the data clearly supports a non-linear I-V relationship, it is, however, not constant. The samples appear to fluctuate from a non-linear behavior to an ohmic behavior and then back to non-linear. The insulator region of the curve grows and then contracts as time passes. The slope of the steep current region changes with time. The hysteresis or difference between the trace and retrace fluctuates with time. The threshold voltage changes in time. The curves show asymmetry from the negative region to the positive region (behavior which could be described by the difference in material of the electrodes injecting carriers into the lattice), which too would change. Rarely do the plots show the same parameters. The relationship of current to voltage is changing from curve to curve. The results reported by Dong *et al* indicate that the current behavior seen in their setup is fairly consistent from cycle to cycle; which

would agree with the suggestion by Waser *et al*[1] that the filaments grow and are destroyed along the same path.

The results reported in this work show this system is not behaving in an expected manner which is inconsistent with SCLC theory and the theory of a singular filament path. Although the V_{TFL} has a higher occurrence at $\pm0.32V$ (Yang *et al* reported a V_{TFL} of .35V [21]), it changes from cycle to cycle and sample to sample. This threshold voltage indicates a potential barrier that the charge carriers must overcome before increased current is measured. This barrier could be described as space-charge barriers (consistent with Schottky barriers etc.), surface traps, or a combination of barriers. If these threshold voltages are indeed due to space-charge barriers, the fluctuation in voltage would suggest the system's band structure is changing from cycle to cycle and that the current does not flow along the same path or that the path changes; therefore, different models to describe the system should be explored.

4.   Mixed Ionic-Electronic Conduction

Because the film is estimated to be very thin and the electric field would be very large, this barrier might also be evidence of a threshold at which point mobile Cu^+ ions begin to move within the lattice creating a peak in current. This is consistent with the model of fast ion conductors in solid electrolytes. The data collected in this work shows similarities to that collected of a CuBr system that was demonstrating the effects of mobile Cu ions within the CuBr film [22].

Voltages applied across films of nanometer thickness have exhibited mobile ions within the lattice. Various descriptions have been used to model the behavior of ionic

conductors. A hopping model describes a situation where static lattice defines a periodic array of vacancies/interstitial sites into which mobile ions may occupy. The ions continue to move to nearest-neighbor vacant sites (to include interstitial sites) via a random walk under the applied electric field. The hopping model requires the ions to be momentarily stationary and therefore excludes oscillatory behavior that is at times observed. This introduces a continuous diffusion model that describes the mechanism as a particle "freely" moving through the medium but taking into account scattering events due to the lattice. Another model describes the conducting ions as a "lattice gas" dictated by its interactions with the static properties of the lattice. The model uses a Hamiltonian to specify the various energy configurations of the vacant lattice sites. Therefore this "gas" could be "excited" into different lattice configurations [23].

Isolating the contribution of ionic conduction from electronic conduction would appear difficult. Many models and theories, however, would suggest the conducting ions are less mobile than the conducting electrons. This allows the use of impedance spectroscopy to isolate the ionic contribution. Impedance is the opposition to alternating current (AC). Under an AC field the electrons show quick response to the changing polarity while the ions would lag behind. This lag is used to identify the conducting ions in impedance spectroscopy.
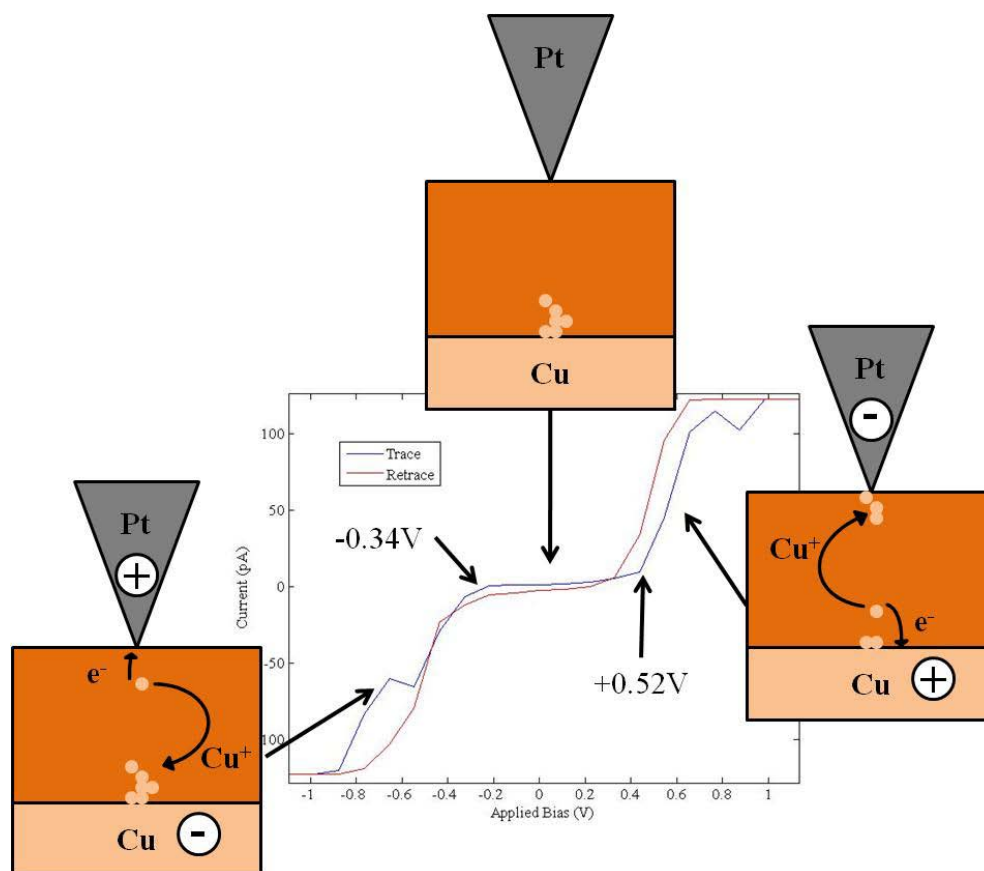
Figure 13. 60 minute sample, 10pA/V current sensitivity. Illustration shows mobile ions hopping through Cu₂O lattice forming filaments. The flow of ions shows correlation with the electrochemical potentials of Cu at ±0.34V and ±0.52V.

With mobile ions the system could be viewed as an electrochemical cell with electrochemical reactions occurring (see Figure 13). Oxidation and reduction could be occurring at the anode and cathode respectively. This model is in agreement with the model of filament growth; as reduction takes place at the cathode (the tip is the cathode when a positive bias is applied to the sample chuck), a build-up of copper will occur as the Cu^+ ions in Cu_2O are reduced. This build-up of copper is analogous with the growth of a filament. This process will reverse as the polarity is changed. This model is confirmed by the histogram analysis for the threshold voltages at which point current increases rapidly. The electrochemical potential for the creation of Cu^+/Cu^{2+} from Cu(s)

31

is .34V and .52V (see equation (9)) respectively—peak currents occur most frequently near these voltages indicated by the histograms (Figure 14 and Figure 15). The slight shifts in threshold voltage to higher voltages as oxidation time increases might be due to the thicker oxide layer or slight changes in stoichiometry thus increasing the potential barrier.
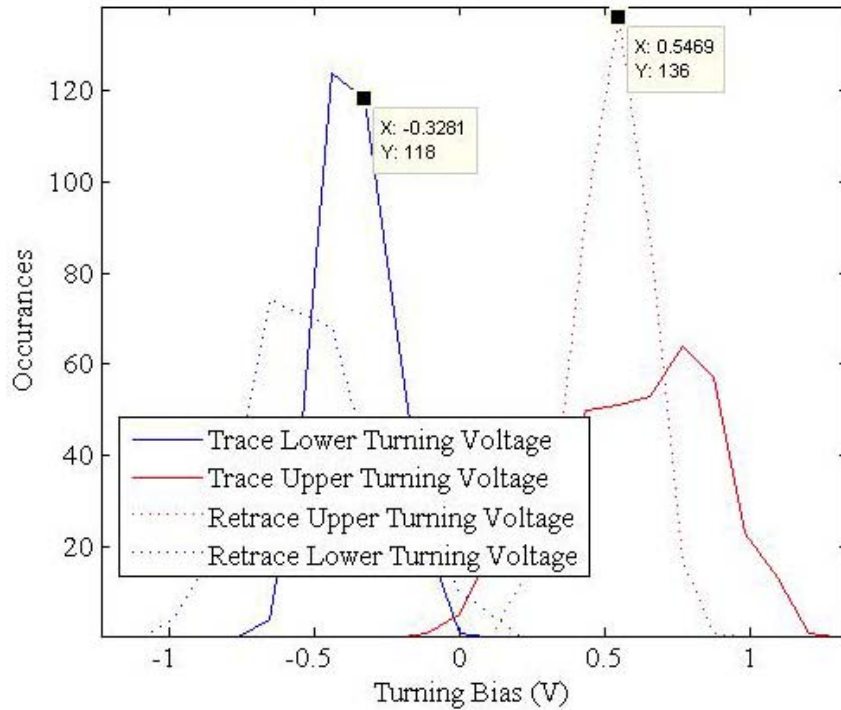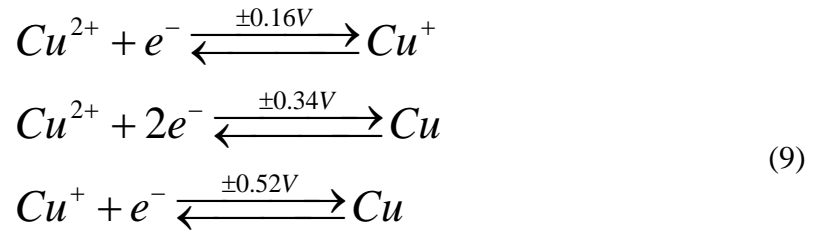
$$Cu^{2+} + e^- \xrightleftharpoons{\pm 0.16V} Cu^+$$
$$Cu^{2+} + 2e^- \xrightleftharpoons{\pm 0.34V} Cu \tag{9}$$
$$Cu^+ + e^- \xrightleftharpoons{\pm 0.52V} Cu$$

Figure 14. Number of occurrences of the critical voltage vs. applied bias for the 10 minute sample at 10pA/V current sensitivity
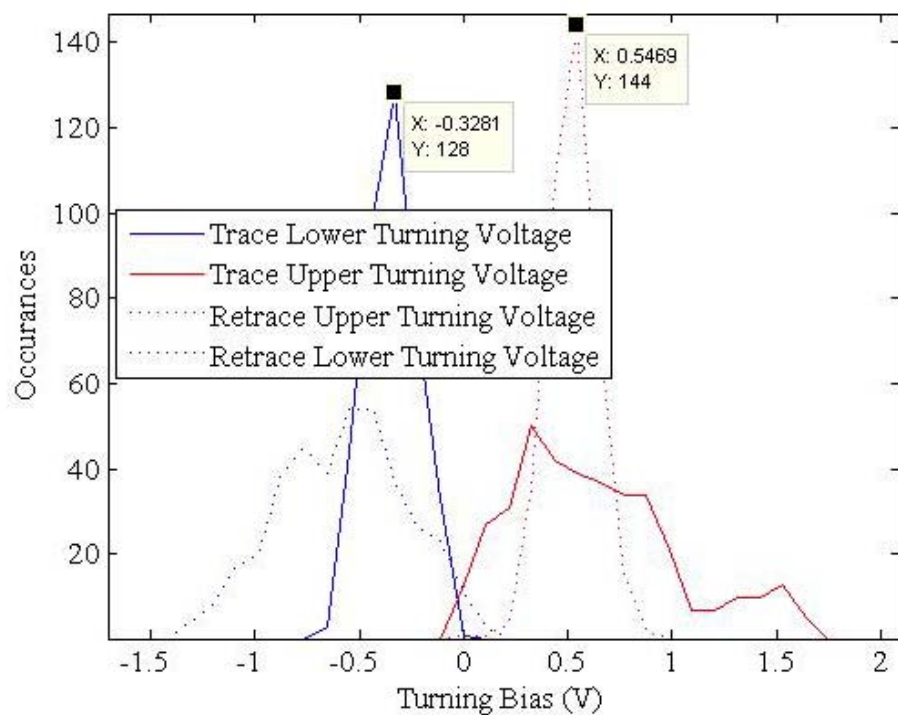
Figure 15. Number of occurrences of the critical voltage vs. applied bias for the 15 min sample at 10pA/V current sensitivity
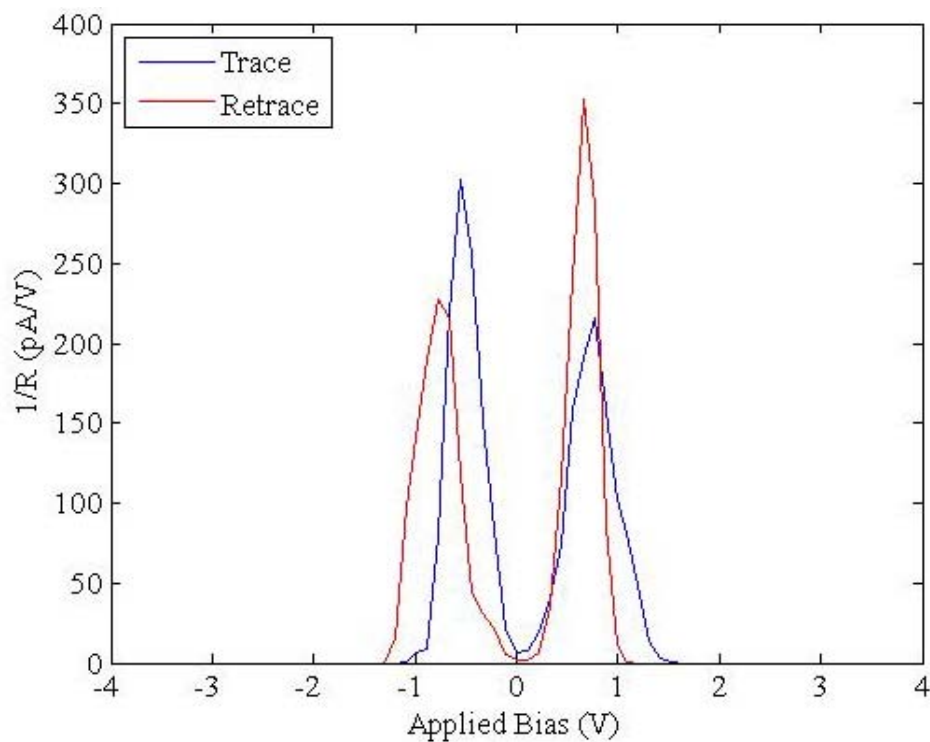

Figure 16. Average conductance vs applied voltage for the 15 min sample measured at 10pA/V current sensitivity.
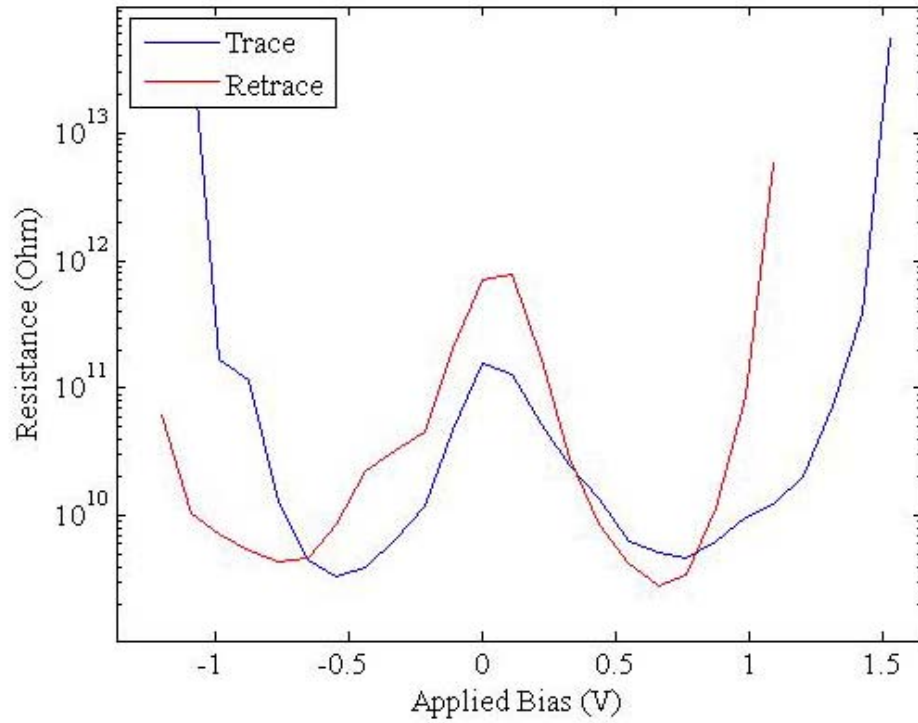
Figure 17. Average resistance vs applied voltage for the 15 min sample measured at 10pA/V current sensitivity.

Neither the curvature of the non-linear region nor the slope of the steep current region is constant. Figure 16 shows the average conductance of all 76 captures taken at each of the five locations for the 15 minute sample measured at 10pA/V current sensitivity. Figure 17 shows the resistance of the same data. Both figures show a common trend of changing properties within the material (if the observed phenomenon is not attributed to the injection of carriers as described by SCLC theory).

$$ - \tag{10}$$

The equivalent resistance must include the gold wire, the gold electrode, copper, and the oxide layer (resistors in series)—all except the oxide layer are assumed constant and have very low electrical resistivity ($\rho_{copper} = 1.68 \times 10^{-8}$ Ω·m, $\rho_{gold} = 2.44 \times 10^{-8}$ Ω·m) and at

34

most a few centimeters in length. Therefore changes in resistance would have to be a result in the changes in the thickness of the oxide layer and/or electrical resistivity of the oxide. Resistance is dictated by the electrical resistivity (ρ) of the material, the area of the contact (A), and the film thickness (l) (see equation (10)). The area of the contact is estimated to be 4.69nm^2 from equations (1) and (2); the area is assumed to be constant as long as the deflection due to the attractive forces of the electric field is minimal. Deflection measurements taken concurrently with the TUNA current ramps showed peaks in deflection on the order of femtometers (10^{-15} m) and therefore negligible. Oxide thickness would change if the system was modeled by filament growth due to mobile ions or if there was an excess in oxidation at the electrodes. This filament growth or oxidation should be no more than one order of magnitude in difference and therefore could not explain changes that are more than two orders of magnitude. Changes in electrical resistivity, a material property, would therefore be responsible for any significant changes in measured resistance, which also could be explained by the changes due to mobile ions.

The samples tend to show relatively similar resistance as oxidation time increases (see Appendix C.3 Resistance). A similar resistivity would imply similar stoichiometry and thickness. Only the 120 minute sample shows marked difference from the other samples in both TUNA current (for the data taken at 10pA/V) and visible color implying a marked change in stoichiometry—possibly evidence of a dominance of CuO on the surface. The small but noticeable resistance change from cycle to cycle evident in all samples is likely due to the change in stoichiometry along the path. It is well known that resistance properties change with preparation techniques for thin films as reported by Rahkshani

[24]. It therefore may be asserted that these small temporal changes in resistance are due to a chemical or structural differences in the current path.

The change in these characteristics from location to location within a single sample could easily be explained by non-uniform oxidation. The problem lies in describing why the characteristics fluctuate temporally. As indicated with the model of the electrochemical cell, the mixed ionic conductor would describe the changes as a system under continuous electrochemical change due to the changing voltage. Many samples showed high conductivity on the first ramp—indicating an ohmic channel—followed by a non-linear and more "insulator-like" retrace (see Figure 18). This could be in agreement with the concept of a conditioning process or forming voltage described in many reports [1]. Many of the samples also show dips in conductivity at particular voltages (shown in Figure 18) which could be an indication of ion movement as these dips often occur at the voltages associated with the electrochemical potentials of copper shown in equation (9).
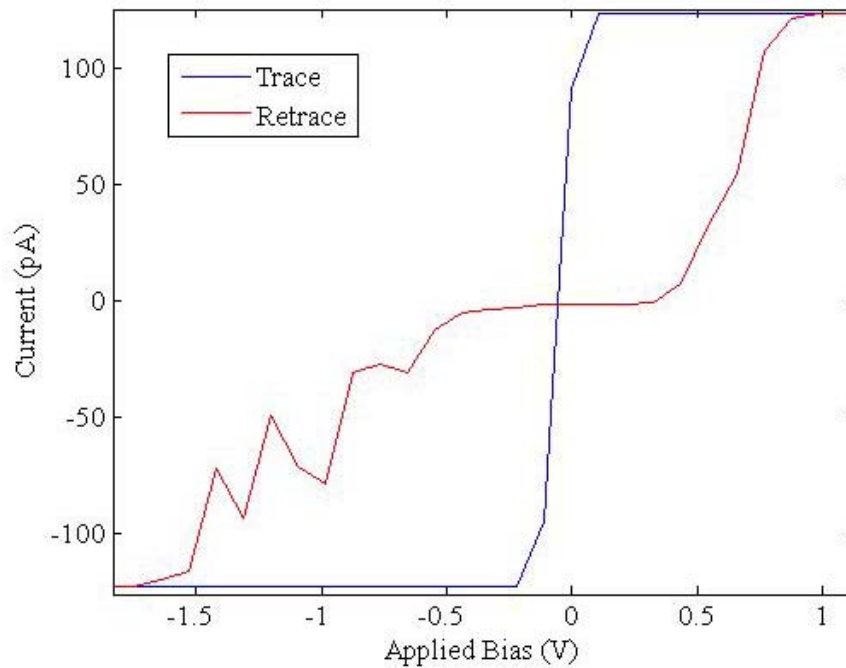
Figure 18. First capture of TUNA data taken on the base sample at the first location. Note the trace begins in an ohmic form followed by a non-linear trace suggesting an electrochemical change in the system. Also note the dips in conductivity in the negative voltage region of the retrace.

Using the base sample as a case-study (see Figure 33 of Appendix C.1 TUNA Results), the first trace in the first capture indicates an ohmic behavior and appears highly conductive. The following retrace in the first capture shows the system has undergone a change to a non-linear system as described above indicating the existence of a low-resistive state and a high-resistive state—illustrated by the trace and retrace respectively. The dips in conductivity in the retrace might be indicative of ion movement as a filament is being destroyed. The next capture shows similar properties but it appears as though there might be ion movement prior to the retrace. Large dips in current flow are very prominent throughout the base sample captures which might suggest this system has a lot more fluctuation due to a higher electric field over the thinner oxide film. Periodically the trace returns to an ohmic behavior which might indicate the tip has thermally drifted

to a new location or the system momentarily has created a stable highly conductive filament which is destroyed in subsequent captures by the movement of ions through the system.

As stated above, the parameters fluctuate from curve to curve for all the samples indicating some structural/stoichiometric change is occurring to cause this change. As time increases the plots show decreases in conductivity—more curvature in the non-linearity and larger "insulator-like" voltage regions—followed by increases in conductivity until the plot becomes ohmic and could be a result of the electrochemical process of filament growth/destruction. This process appears to be cyclical and the period of the cycles seems to increase with oxidation time (see Appendix C.1 TUNA Results). This cyclical behavior might be evidence of thermal drift of the TUNA tip indicating the tip has moved slightly (<1nm) to a location where the path is more conductive or a new filament path must be established. The period would increase as oxidation time increased due to either less ability to drift due to surface structure or the grain boundaries are larger and there are fewer boundaries to drift to. If the tip drifted over a region of many grains, the resulting current data would indicate many cycles of this change in conductivity. As the tip drifts over a sample with fewer grain boundaries, there would be longer periods between changes which are evident in the data.

Another possible explanation for this fluctuation in the curves is the path of least resistance is created randomly as ions overcome potential barriers and migrate to vacancies within the lattice. A cyclical undertone in the data would therefore be evidence that the change in the number of migratory ions decreases momentarily due to the

38

environmental conditions at that instance. Looking at an overlay of all data from a sample taken at one location and comparing these plots to each other it can be seen that the distribution of paths changes with oxidation time (see Appendix C.2 TUNA Results). For the low-oxidation samples the distribution of paths varies considerably. As oxidation time increases it appears as though the variation in path distribution decreases. This suggests there are fewer paths available or the paths are more similar lending to more similar current measurements. As indicated above the contact radius is estimated to be roughly 1.2nm and particle sizes are estimated to be >8nm from AFM scans and particle size calculation reported in other works. This creates a situation where the tip could overlay a number of configurations of grains boundaries and that number would likely decrease as particle size increases. Presumably the path of least resistance would be along grain boundaries. The particle size on the surface tends to grow in size with oxidation time and changes the distribution of grain boundaries. As the number of grain boundaries decrease with increasing particle size, the number of paths available for current flow decrease making the variation in current measurement decrease.
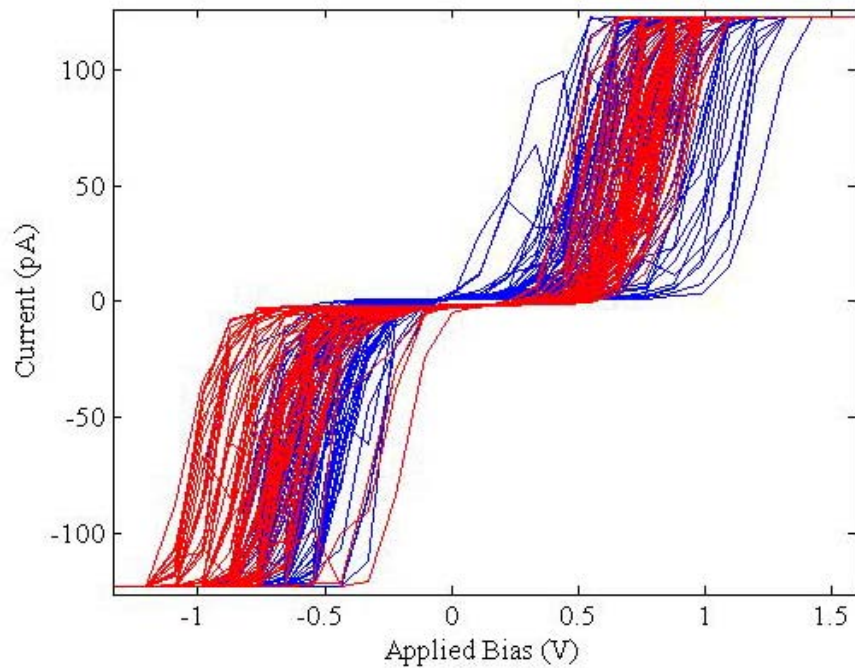
Figure 19. Tuna data for the 15 min sample at 10pA/V current sensitivity for all 5 locations and 76 captures at each location. Trace data is shown in blue and retrace in red. Overlay of data highlights the distribution of current behavior. Narrower distributions indicate less available paths for current to follow.

Another interesting feature is the change in the insulator region. It appears as though the curvature in general increases and peaks at the 15 minute oxidized sample in which there is a very distinct and relatively large insulator region (see Figure 19). The 45 minute sample doesn't show as distinct a region, with the 60 minute sample having curvature similar to the 5 minute sample (the 30 minute sample shown is atypical; the other locations sampled show increased curvature). Looking at the reflectance data it is noticeable that there is a peak that begins at ~420nm in the 135 second sample and grows in relative intensity compared to the other peaks as the oxidation time increases. This peak's relative intensity is highest for the 15 minute sample at ~475nm suggesting this band structure is the dominant factor dictating the form of the I-V curve. The peak is at a higher energy corresponding to a larger threshold voltage seen in the I-V curve. The

40

relative intensity compared to the peak located at ~650nm gradually reduces for the higher oxidized samples and is at a minimum in the 60 minute sample which has a corresponding reduction in curvature. As indicated before it is believed the peak between ~420nm to ~500nm is due to the growth of Cu_2O nanoparticles on the surface.

IV.   Conclusions and Recommendations

1.   Contributions of Research

This effort highlights the electronic properties of low-temperature thermally-grown cuprous oxide. The TUNA proved to provide highly localized and sensitive results. These results support a random process in current path under the processing conditions followed. Interesting electronic and optical properties of thermally grown cuprous oxide were measured.

The data indicates the prepared system shows a non-linear I-V relationship and hysteresis similar to reported memrisitve systems; however, it does not support the concept of a singular filament path. The data may be more representative of a system described by mixed ionic-electronic conductors within a solid electrolyte where mobile copper ions move through the lattice under the influence of the strong electric fields. The electronic behavior appears to follow a random process but shows a periodic temporal fluctuation and indicates the behavior is dependent on grain boundary distributions and oxidation state. Distribution of the I-V curves highlight this dependence on grain distribution, namely the fewer the grain boundaries in contact with the electrode, the more controlled the electronic properties respond.

Ion mobility shows correlation with the electrochemical potentials of copper. A histogram analysis of threshold voltages correlates to the electrochemical potentials of copper in an electrochemical cell. The I-V relationship is similar to those reported in efforts highlighting fast ion conductors indicating a similar phenomenon is likely.

In correlation with reflectance data, the I-V data suggests band structure from surface particles can impact the electronic behavior as indicated in the 15min sample. Reflectance data and AFM scans collected also indicate nanosized particles are growing on the surface and have a quantum effect on the band structure.

2.   Significance of Research

This research shows some benefits of the capabilities of the TUNA and explores the novel electronic properties of thin film cuprous oxide. It confirms the non-linear I-V properties and hysteresis common in thin films and explores the material properties involved in the process.   This research provides a basis for further research into techniques to identify the mechanisms contributing to memristive and other unique properties in thin film cuprous oxide and its use as a novel electronic device.

3.   Recommendations for Future Research

The data collected in this effort raises many questions for future research. The data reveals many interesting electronic and optical properties of cuprous oxide. Efforts could be made to better understand the effect of film stoichiometry and thickness have on the absorption spectrum which could be supported by x-ray photoelectron spectroscopy (XPS) measurements. Further characterizing the particle growth as a function of oxidation time and determining its effects on the electronic and optical properties of the material. Further pursuits of a memristive device would be best suited by growing the oxide layer from sputtering copper-oxide opposed to thermally growing the oxide. Many efforts have already been made to characterize the electronic properties of sputtered copper-oxide to fabricate.

One method would be to test the electronic properties via a trial and error method with thin film deposition. Create many cross-hatch devices in a sealed environment using a copper oxide target and varying deposition parameters to test electronic properties. Sputtering with copper oxide target may eliminate some variability inherent with thermal oxide growth, but introduces new variability with deposition environment. This would also eliminate the possibility of thermal drift of the electrode associated with AFM tip.

Testing the electronic properties via semiconductor probe station could provide a way of comparing/contrasting the TUNA results and should provide an average response. It would be prudent to characterize the thermal oxidation with ellipsometry, SEM EDS, and XPS to assess chemical states and film thickness. These methods may also provide more evidence of ion migration. Study of a horizontal MIM structure may make it possible to further investigate ion migration. A horizontal M-I-M structure could be made by laying thin conducting wires on a copper oxide surface and then severing the wire with a diamond AFM tip.

Appendix A Reflectance Results
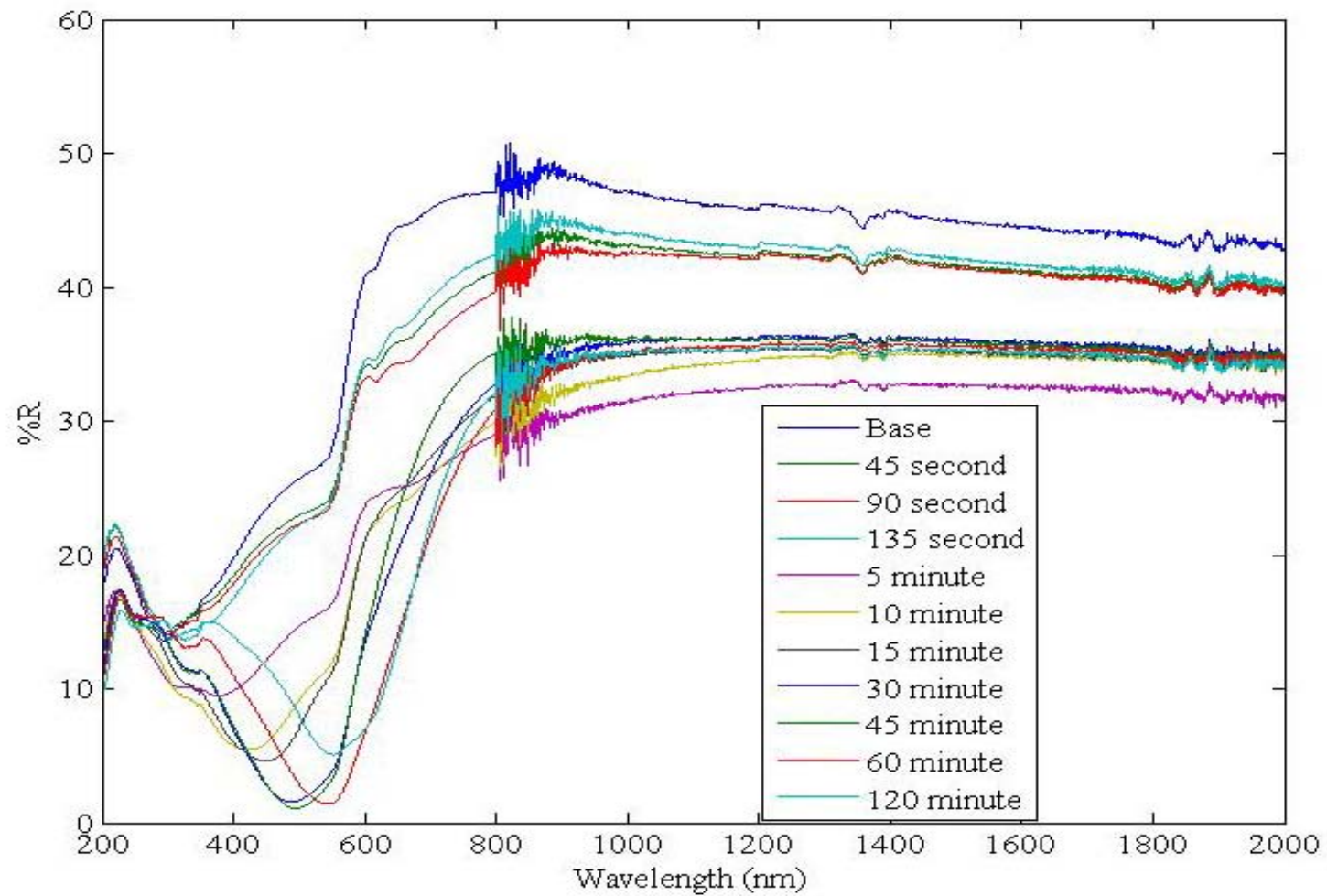
Figure 20. Raw reflectance data
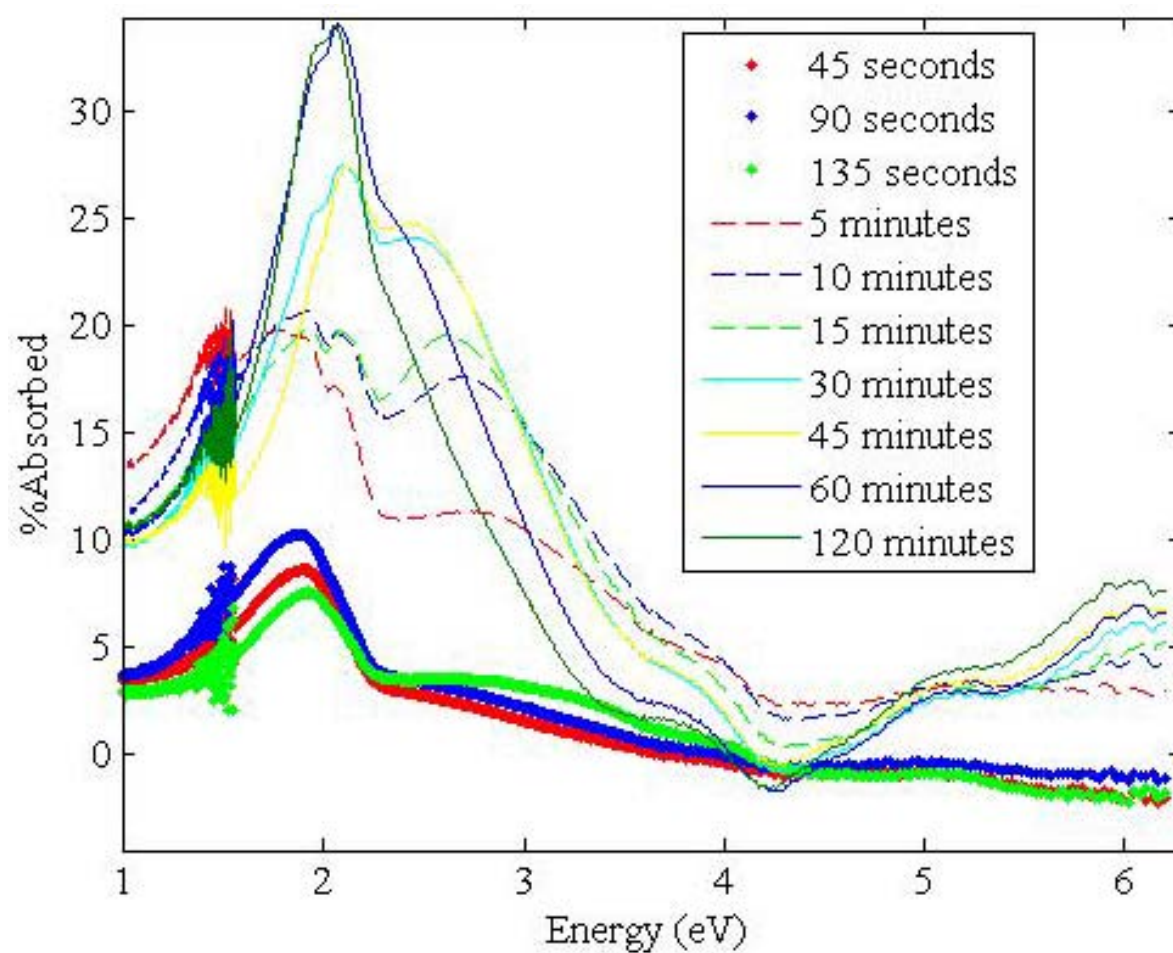
Figure 21. Absorption vs energy

Appendix B AFM Scan Results
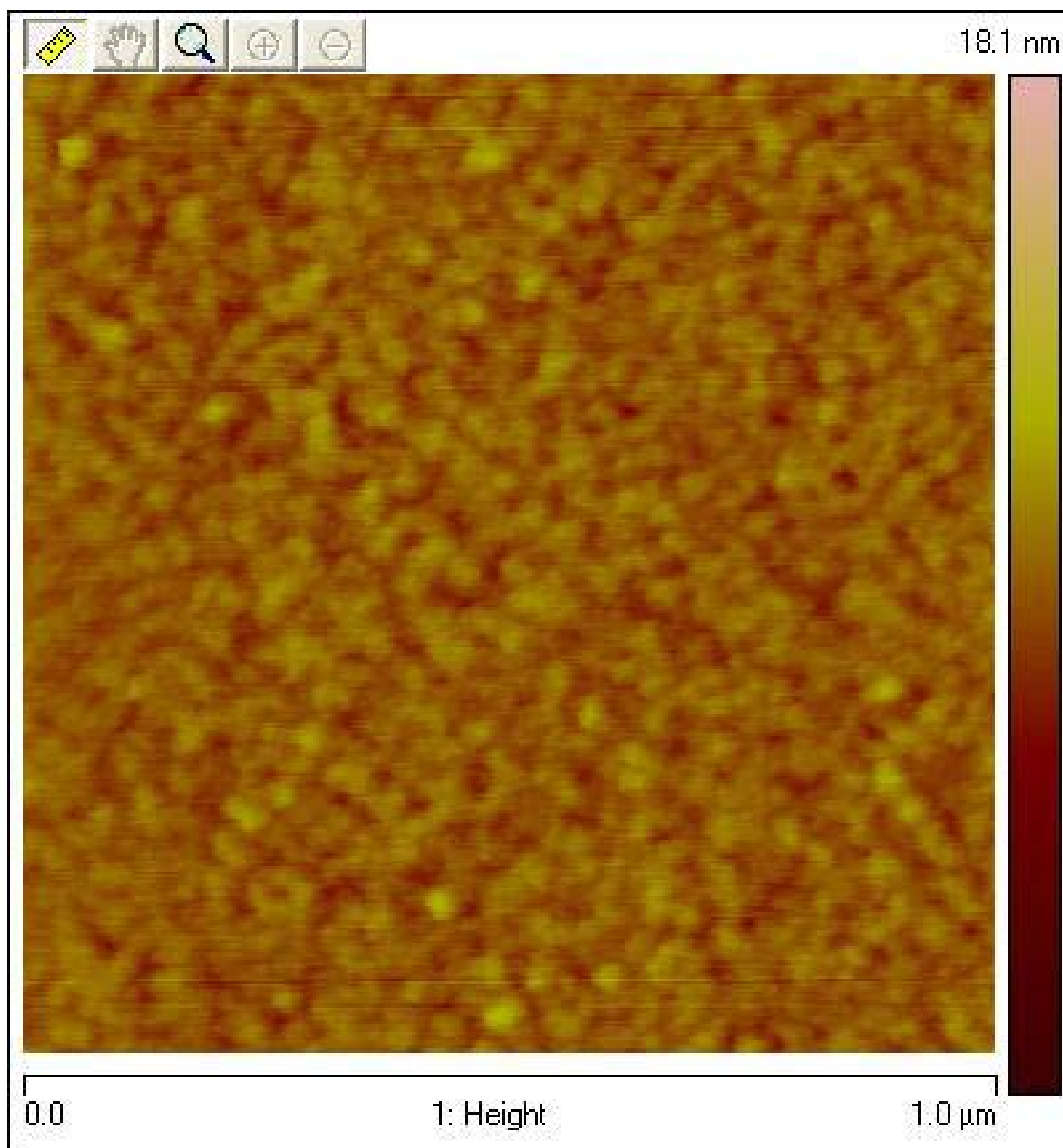
Figure 22. Base sample scan
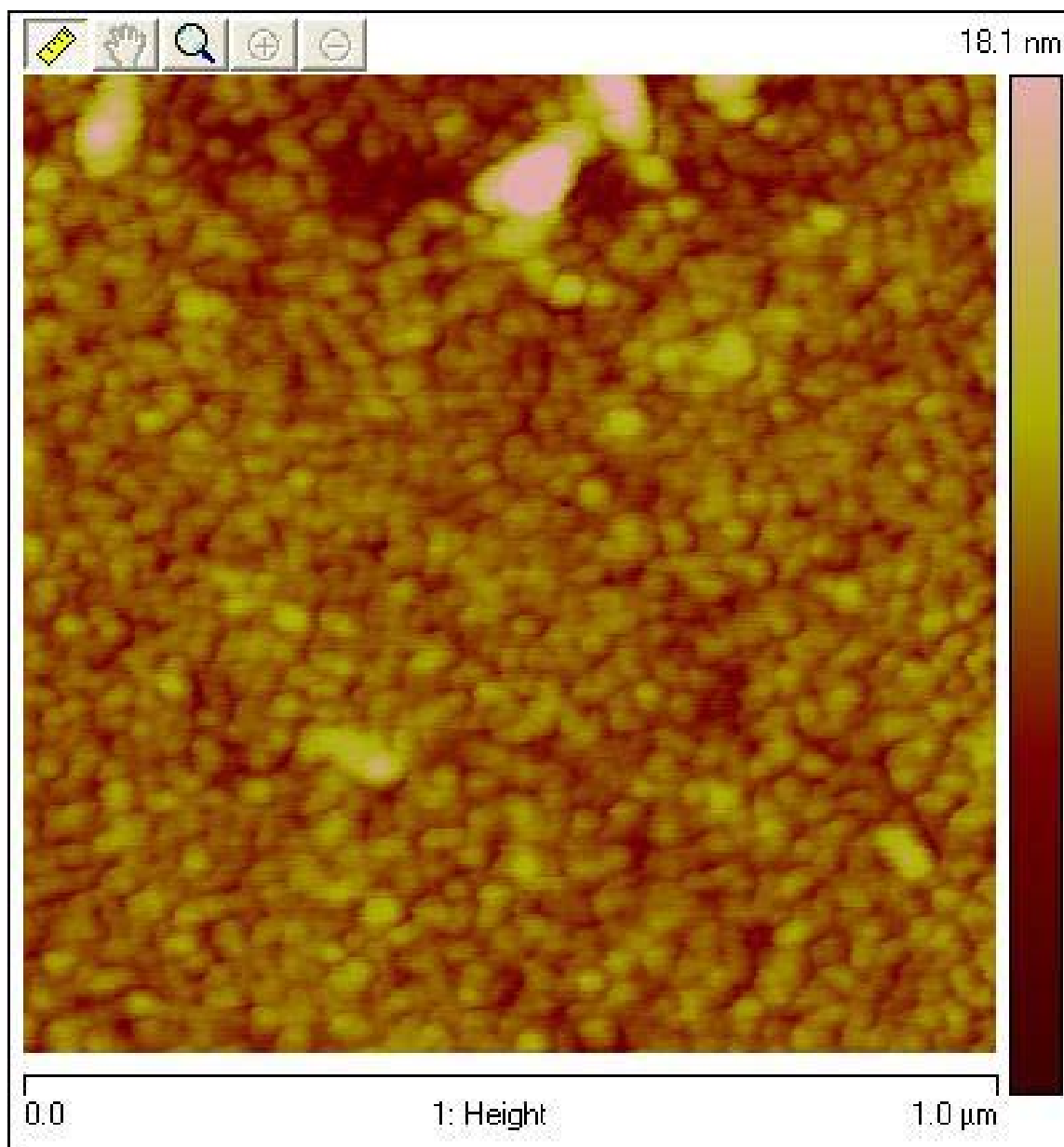
Figure 23. 45 second sample scan
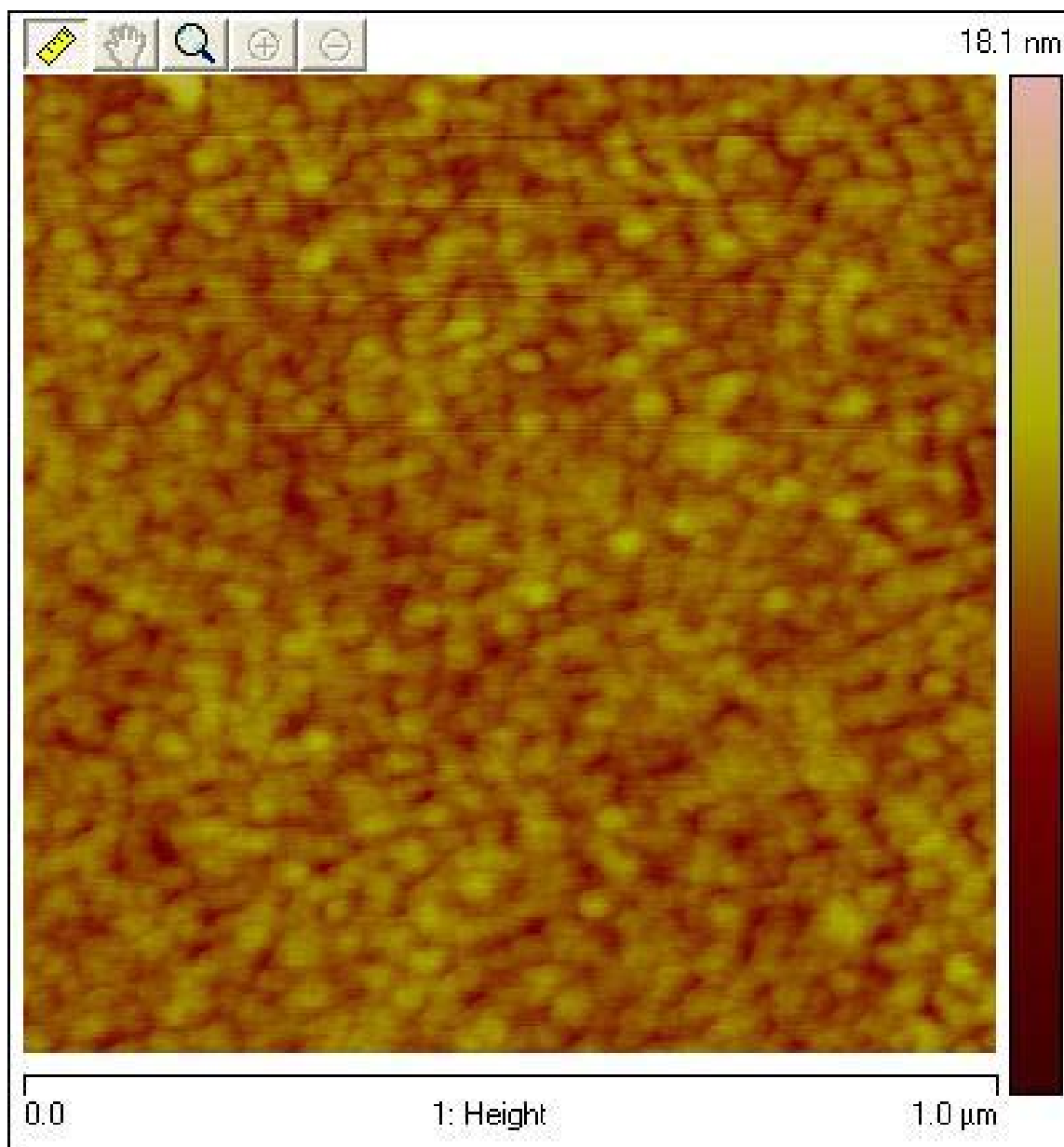
Figure 24. 90 second sample scan
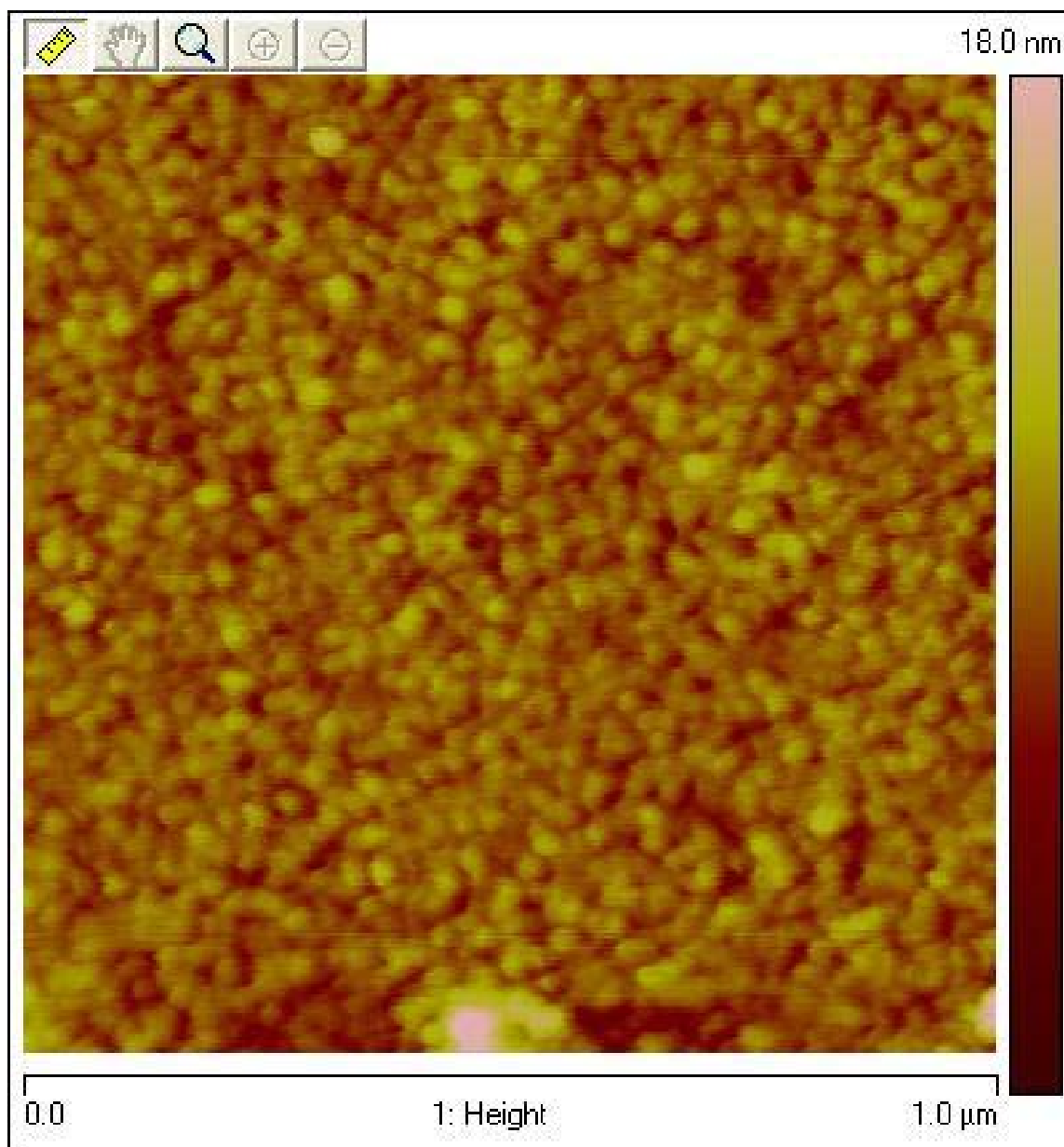
Figure 25. 135 second sample scan

50
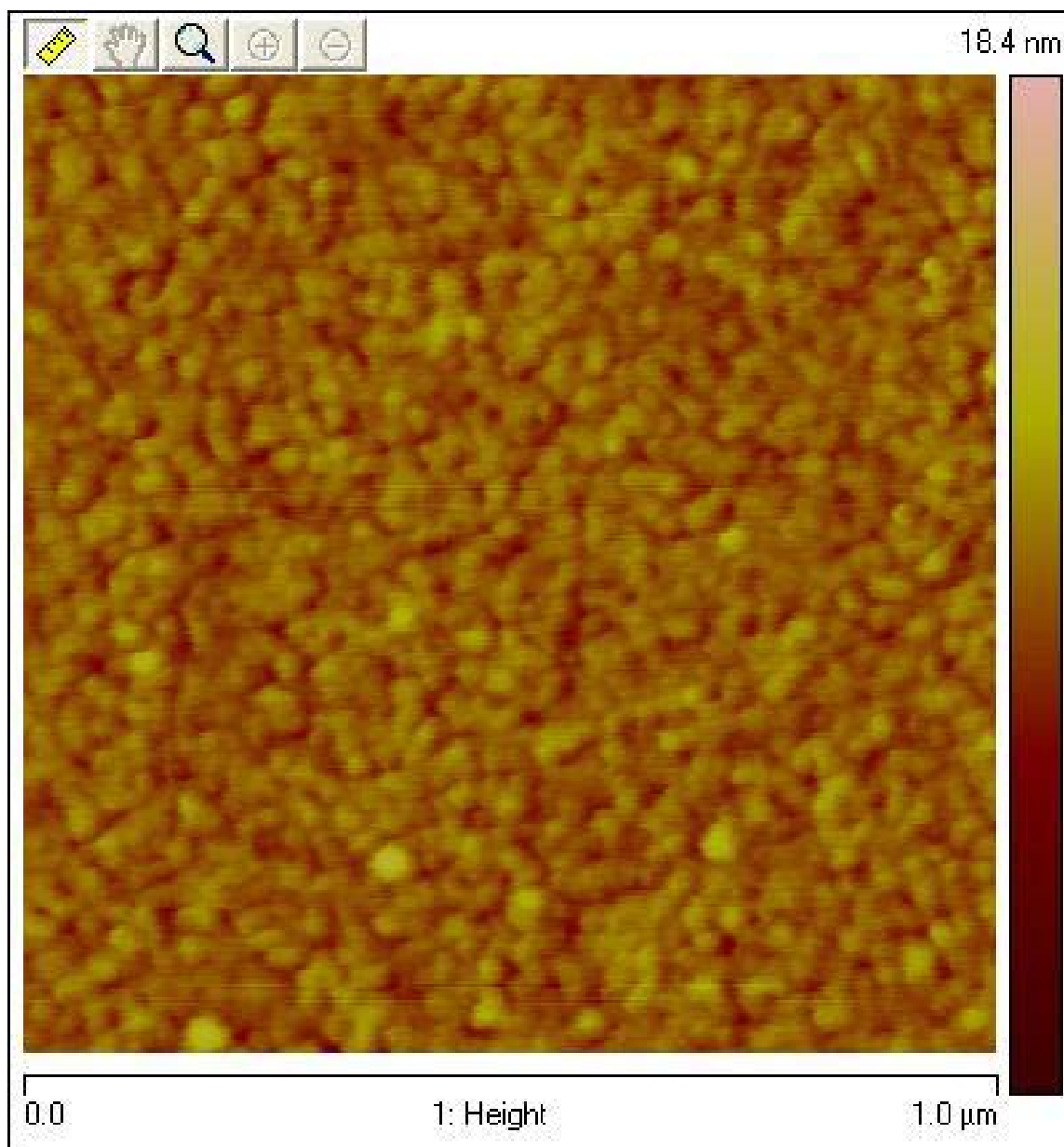
Figure 26. 5 minute sample scan
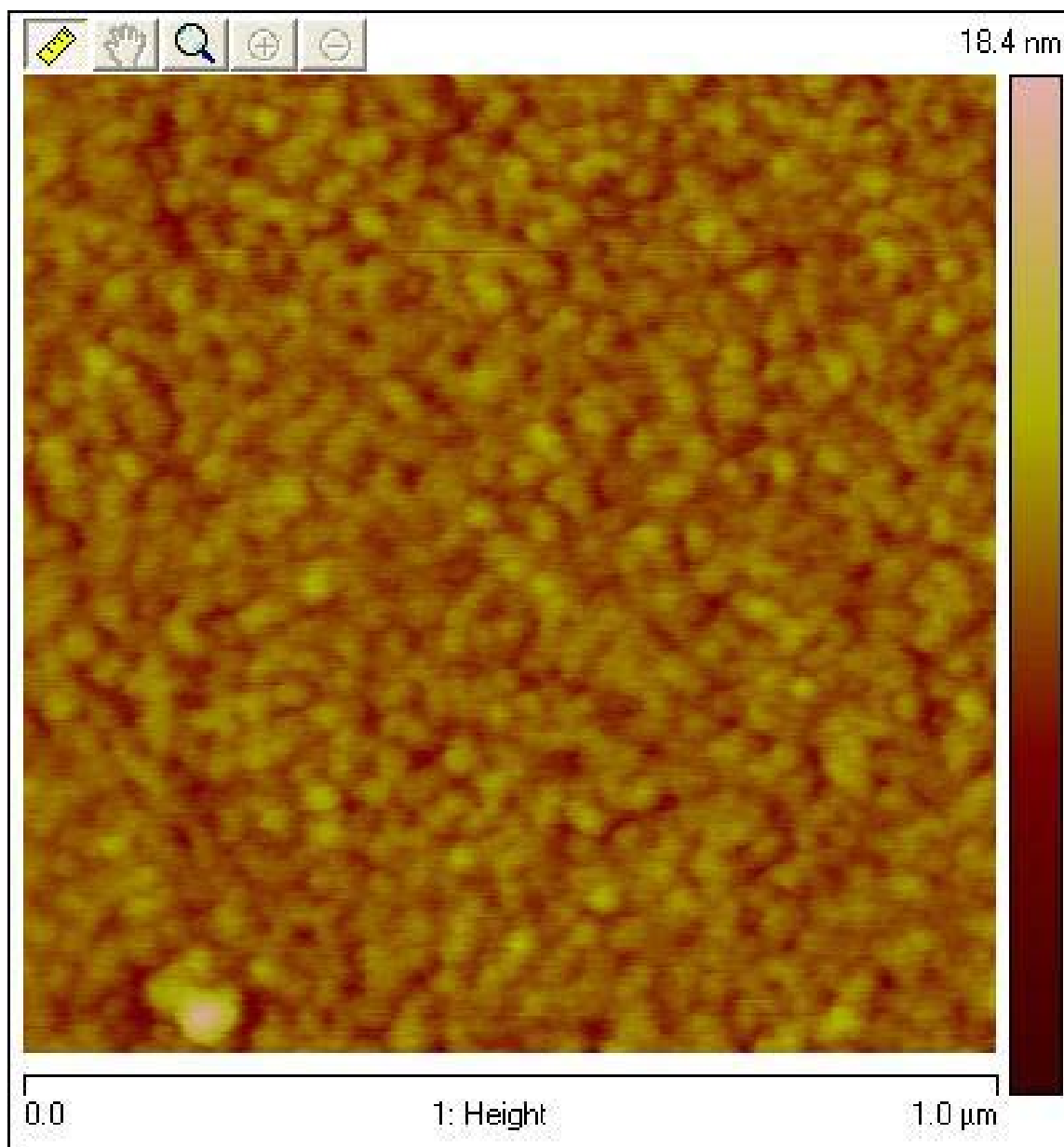
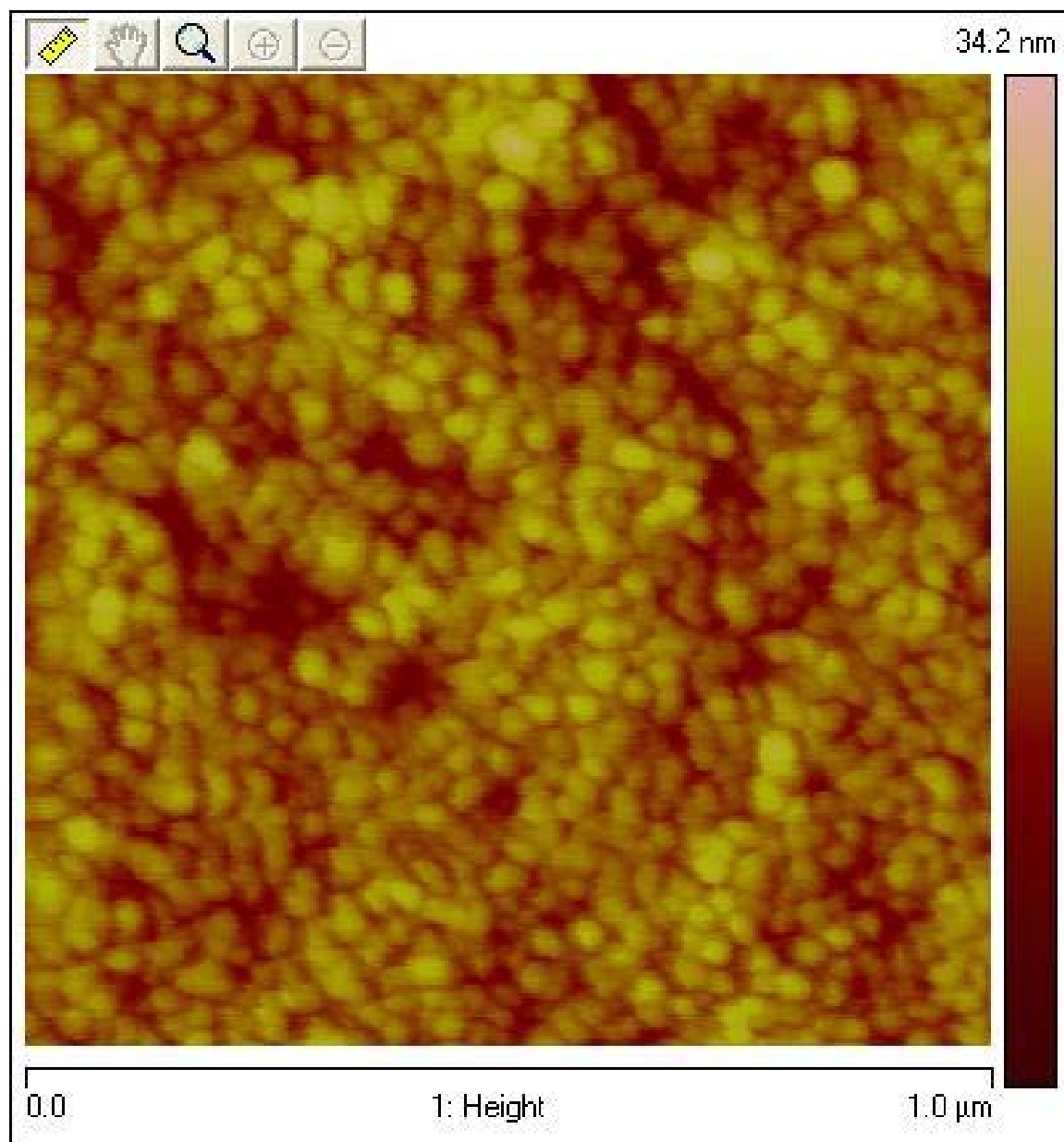**Figure 27. 10 minute sample scan**
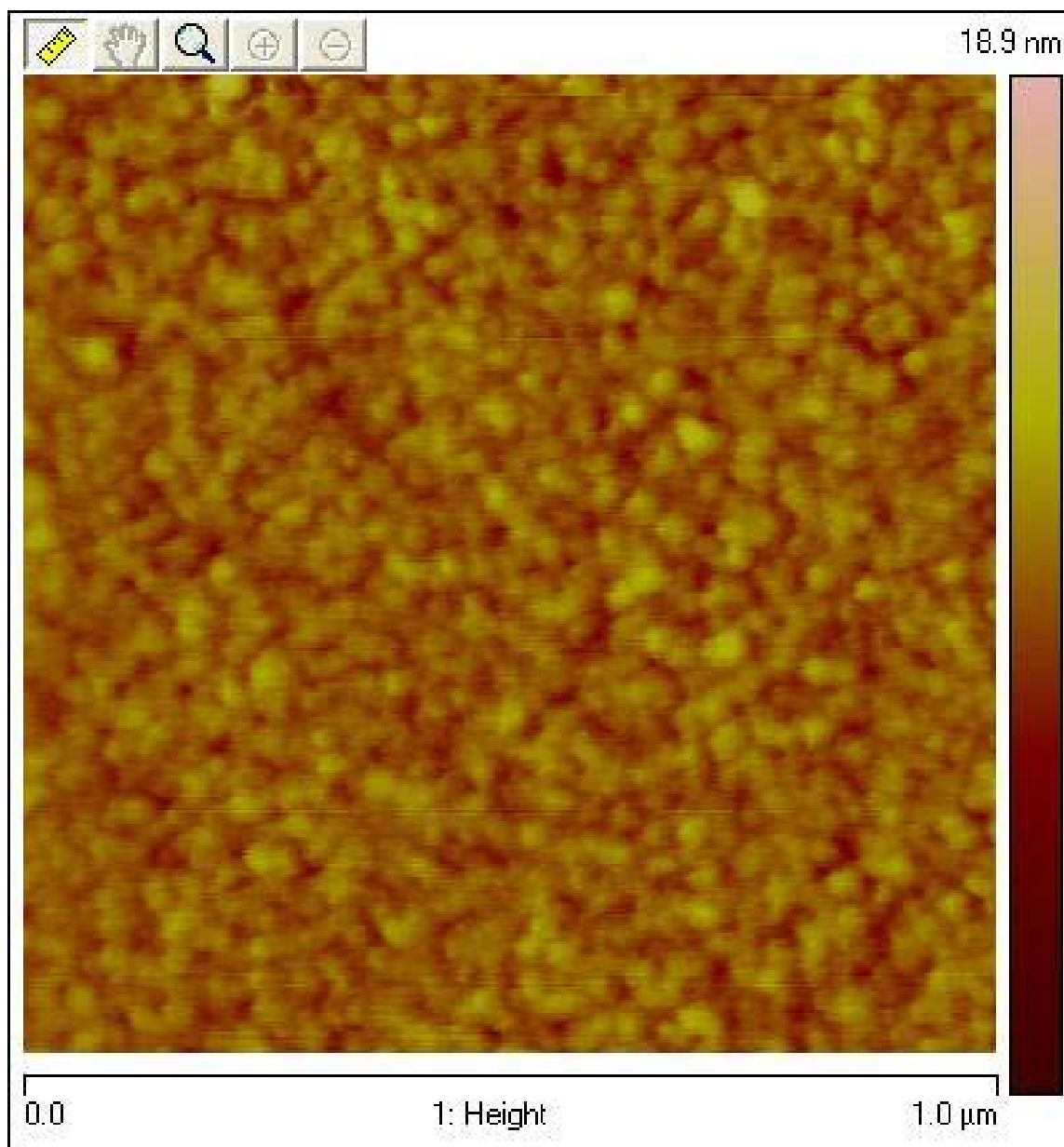
Figure 28. 15 minute sample scan
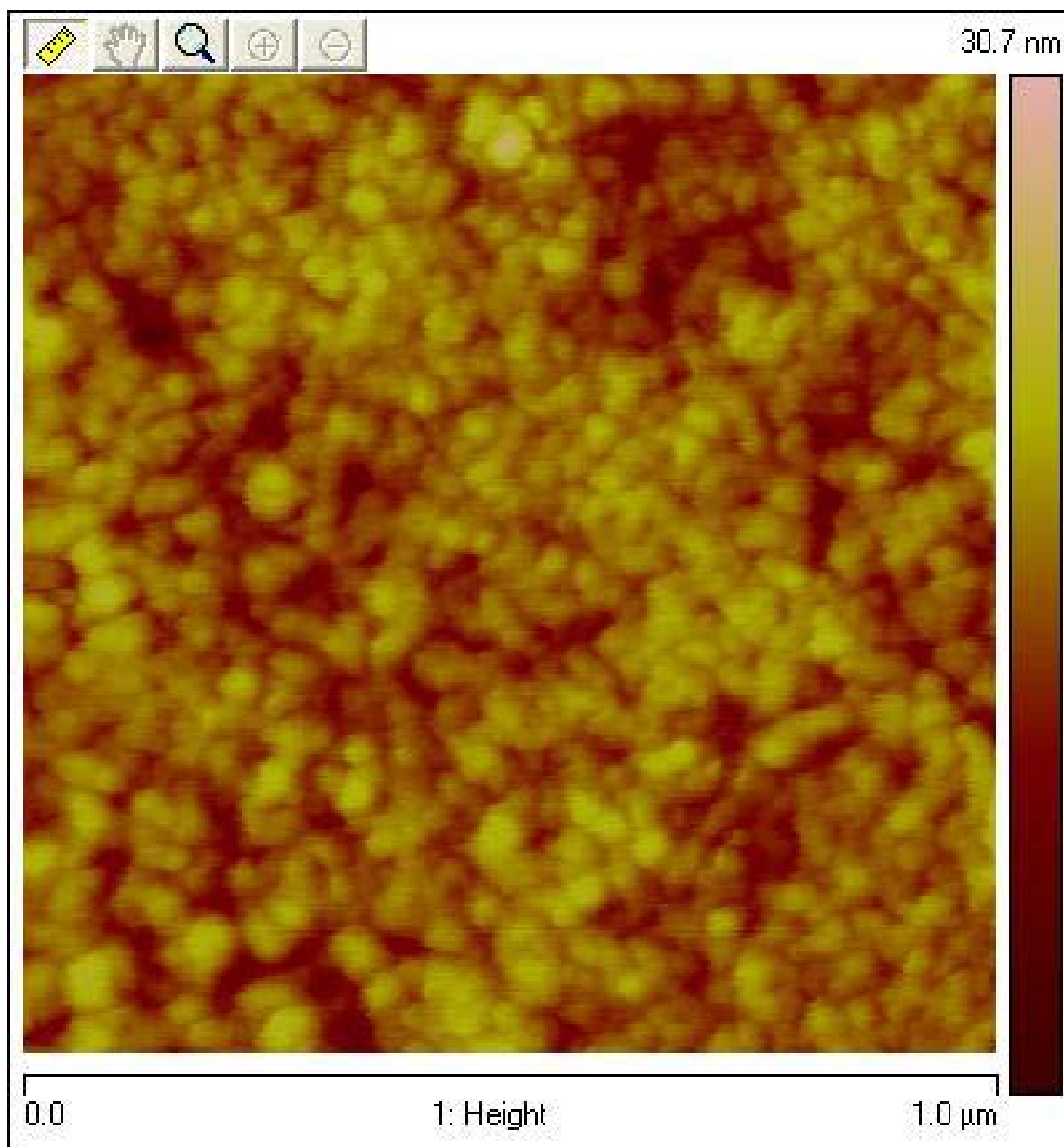
Figure 29. 30 minute sample scan
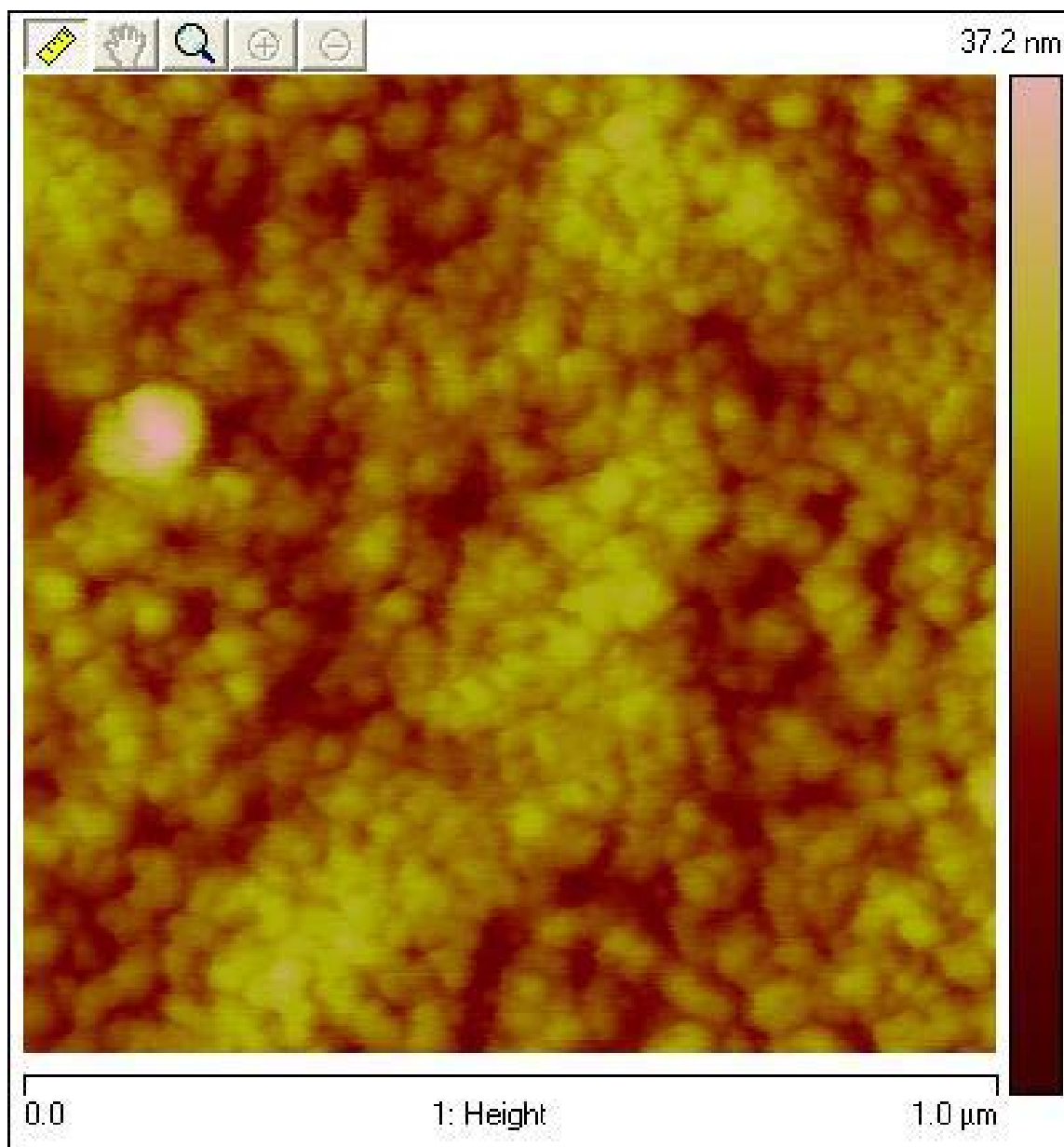
Figure 30. 45 minute sample scan

Figure 31. 60 minute sample scan
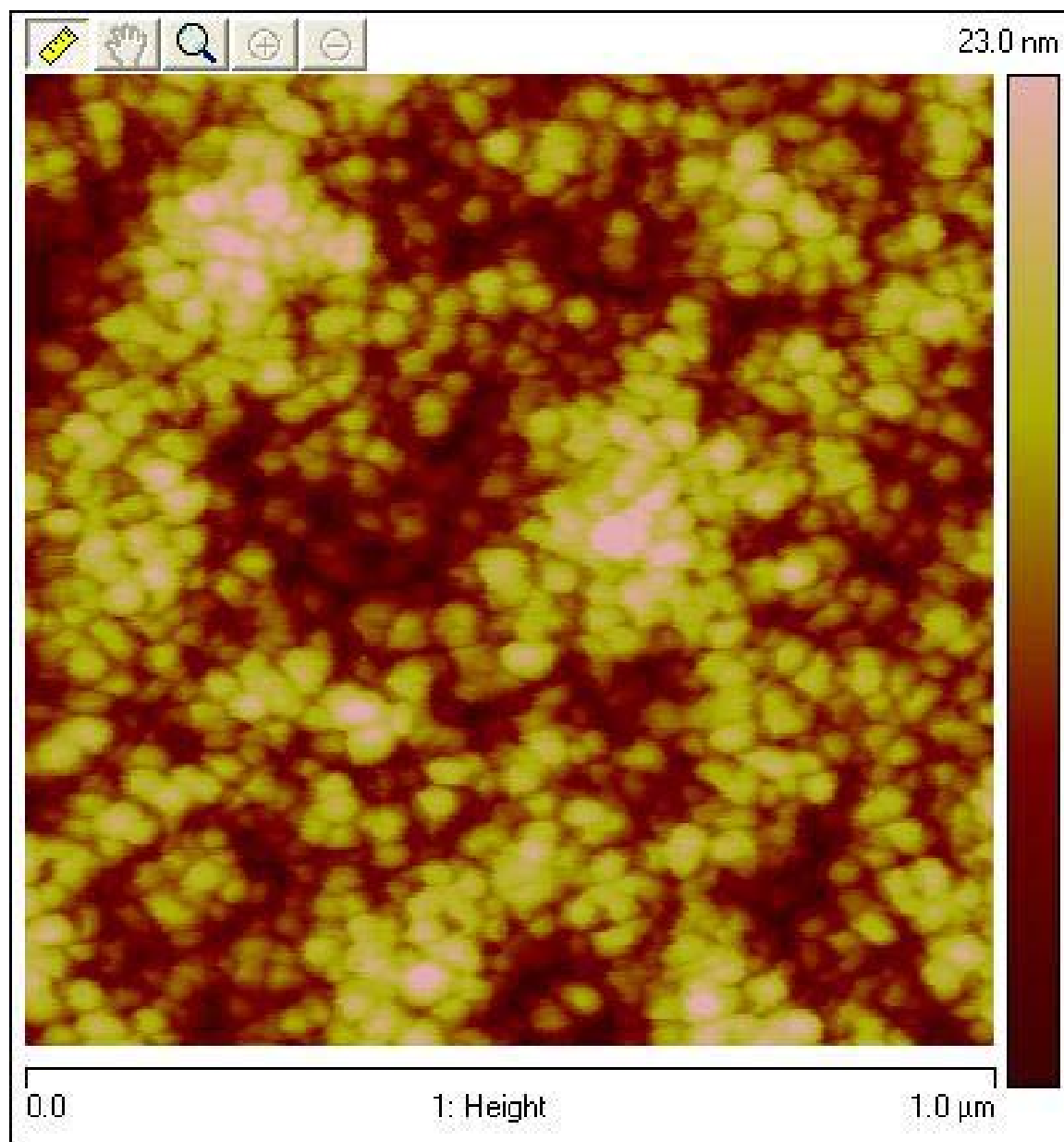
Figure 32. 120 minute sample scan

Appendix C.1 TUNA Results
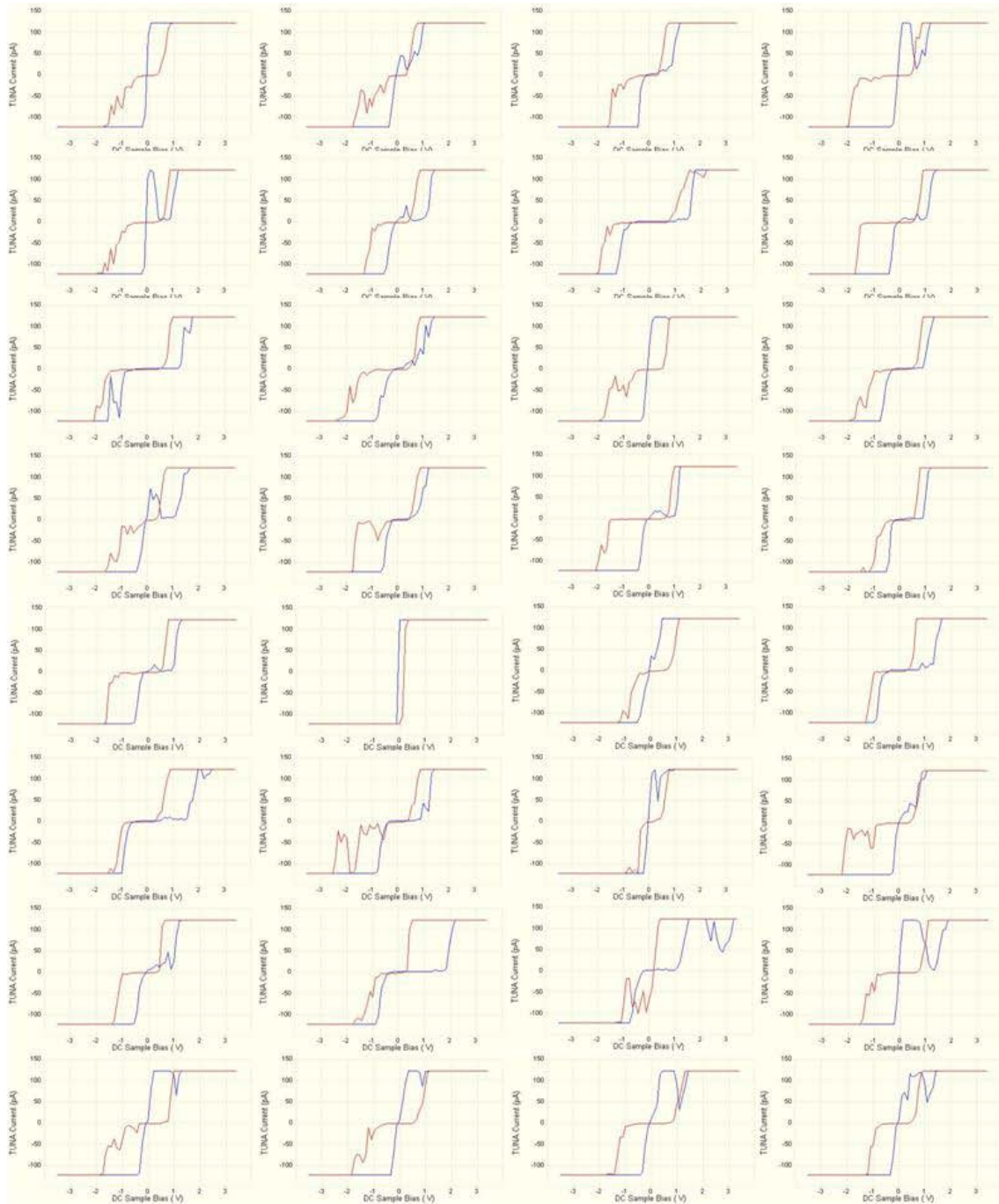
Figure 33. Captures 1-32 of TUNA data of the base sample taken from the first location. Note the fluctuation in parameters, dips in conductivity, and a slight periodicity from non-linear behavior to ohmic and back to non-linear.
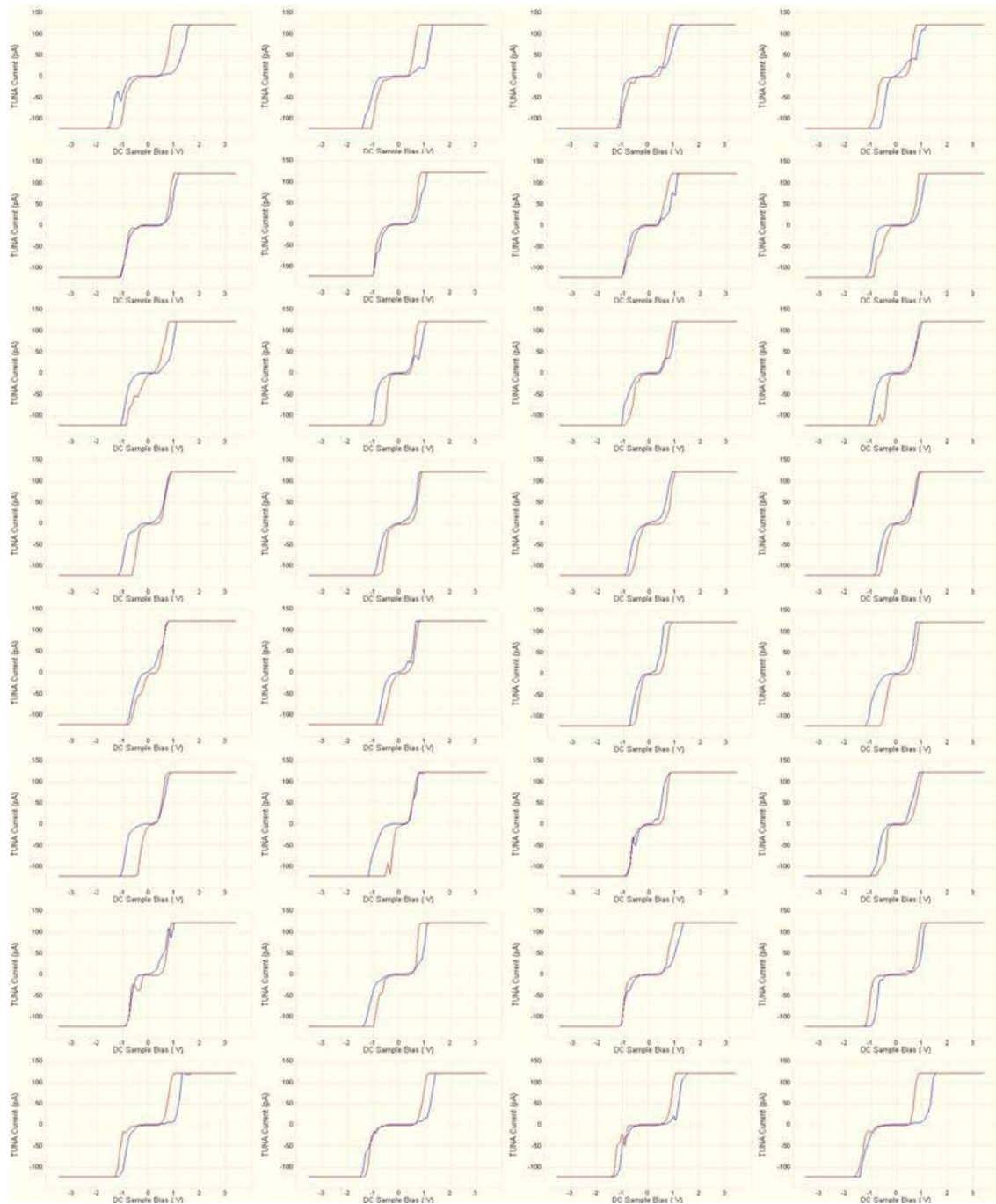
Figure 34. Captures 1-32 of TUNA data of the 5 minute sample taken from the first location. Note the fluctuation in parameters, dips in conductivity, and a slight periodicity from non-linear behavior to ohmic and back to non-linear.
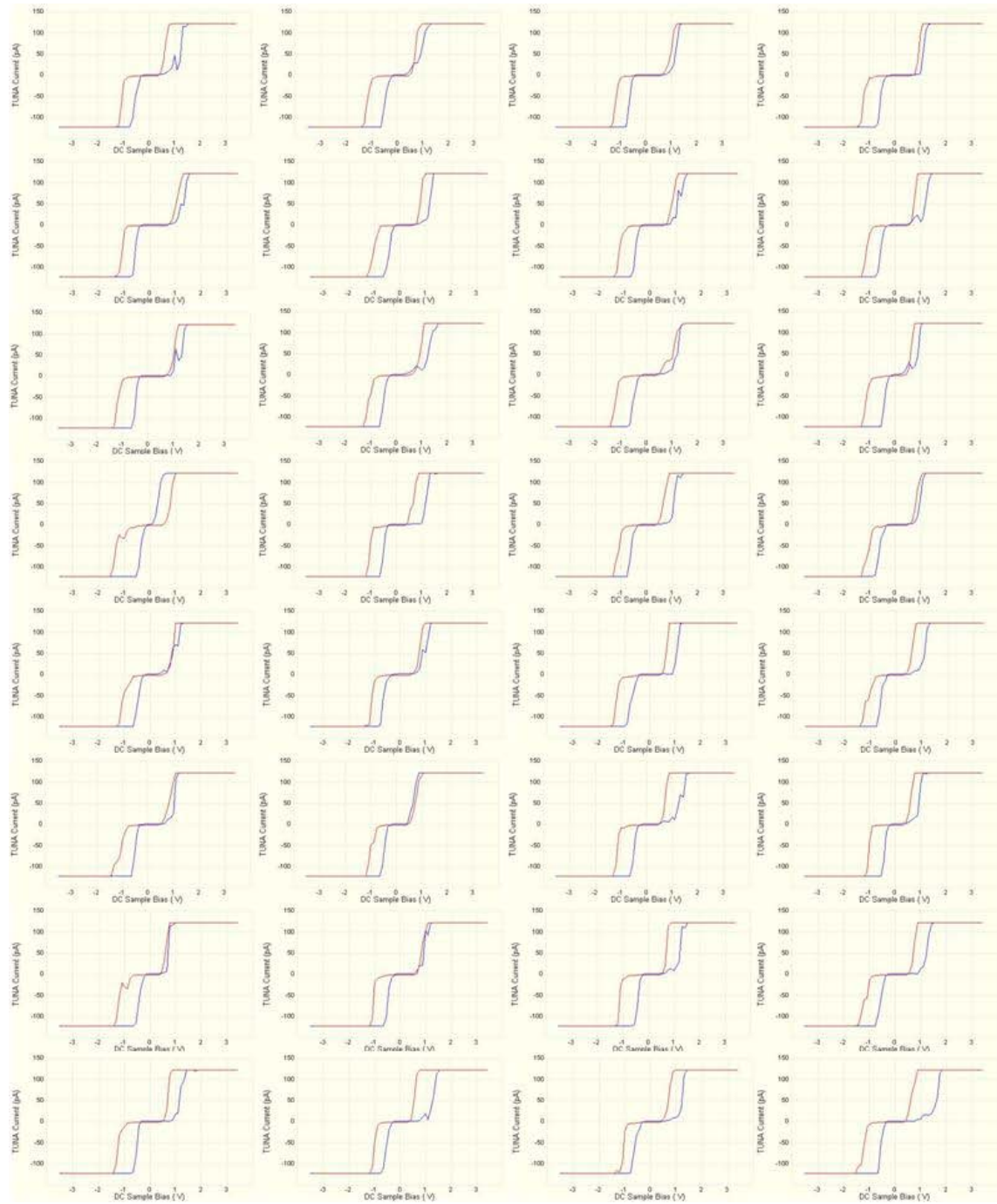
Figure 35. Captures 1-32 of TUNA data of the 15 minute sample taken from the first location. Note less fluctuation in parameters.

60
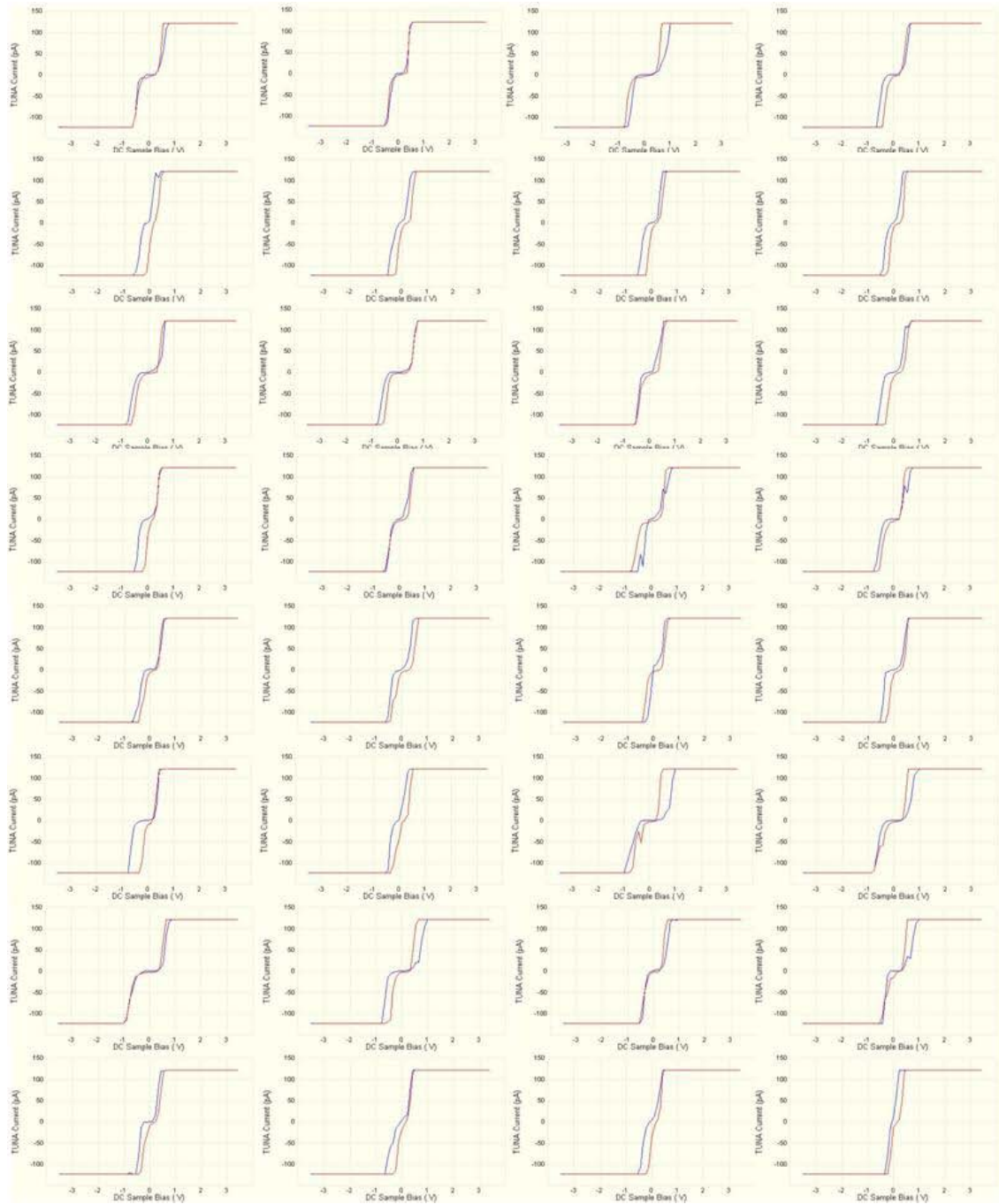
Figure 36. Captures 1-32 of TUNA data of the 60 minute sample taken from the first location. Note the fluctuation in parameters, dips in conductivity, and a change in periodicity from the 5 minute sample. It appears as though the current remains in one state for longer periods of time.

Appendix C.2 TUNA Results
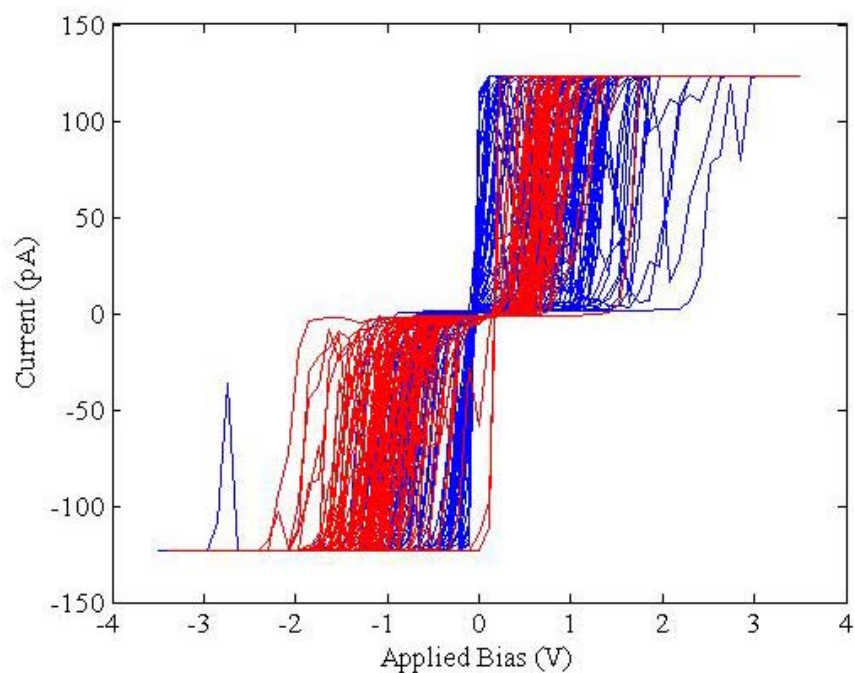
Figure 37. Tuna data for the base sample at 10pA/V current sensitivity for all 5 locations and 76 captures at each location. Trace data is shown in blue and retrace in red.
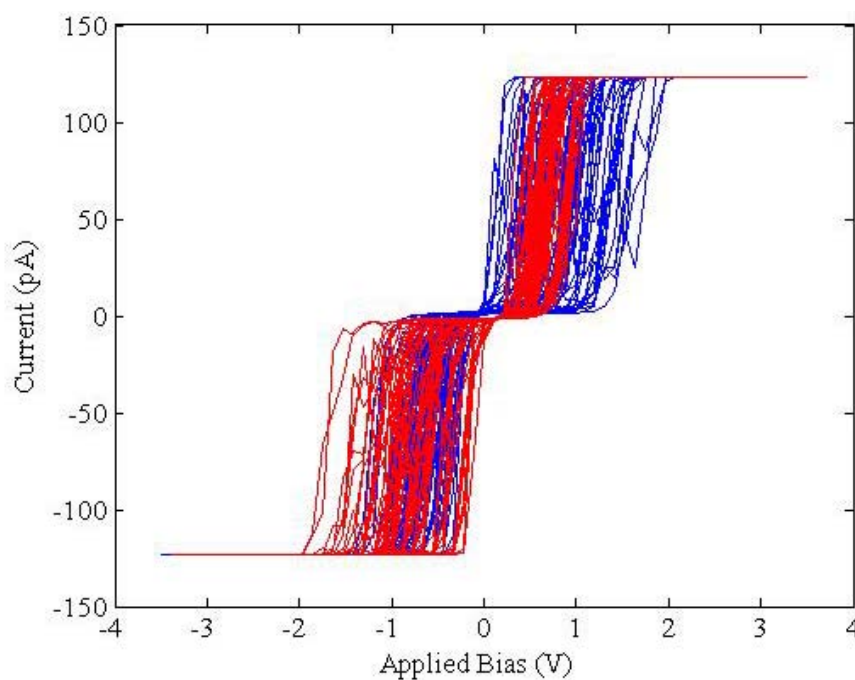
Figure 38. Tuna data for the 45 sec sample at 10pA/V current sensitivity for all 5 locations and 76 captures at each location. Trace data is shown in blue and retrace in red.
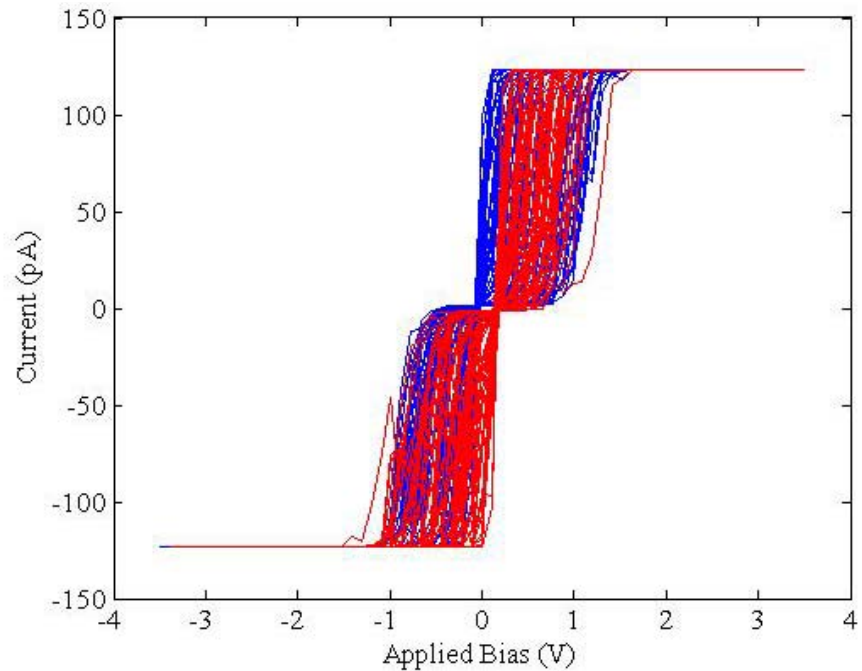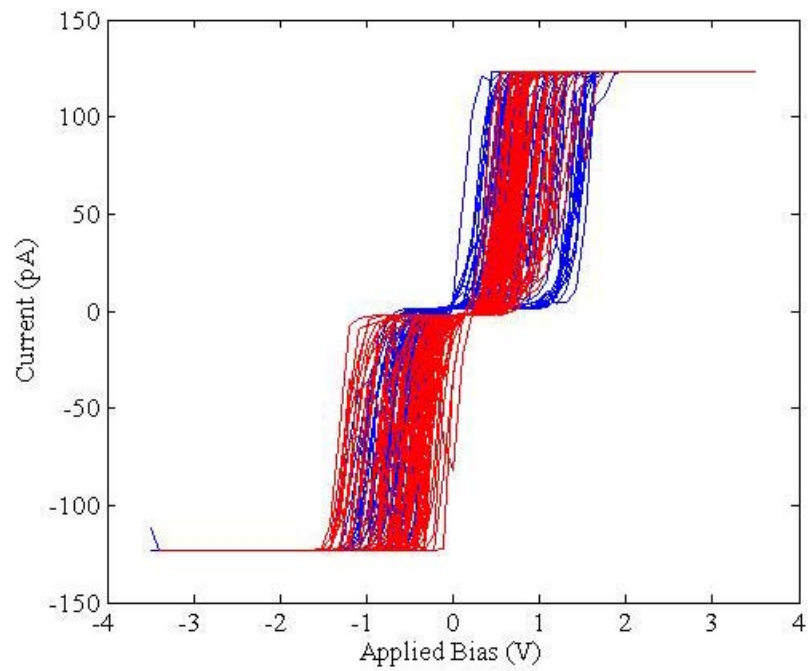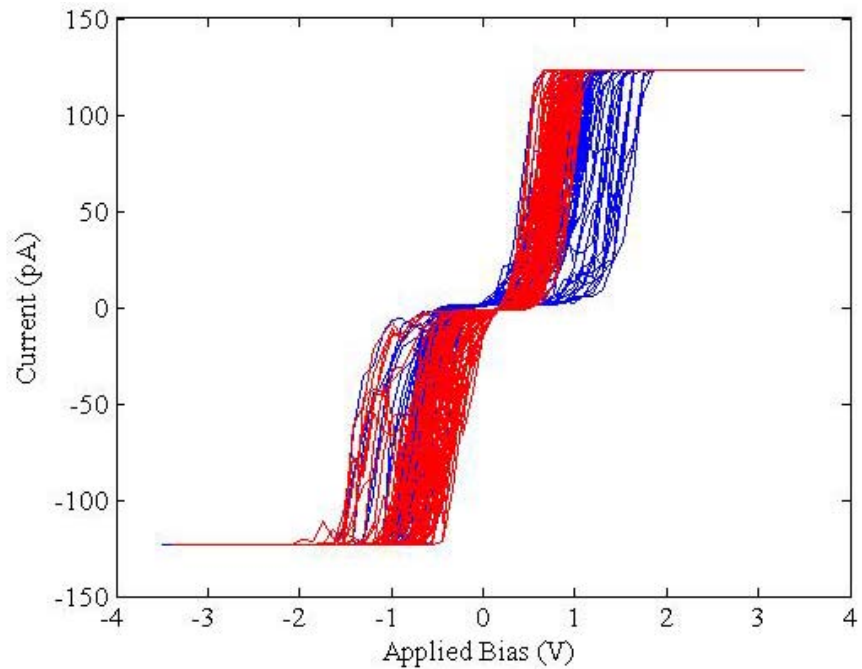
Figure 39. Tuna data for the 90 sec sample at 10pA/V current sensitivity for all 5 locations and 76 captures at each location. Trace data is shown in blue and retrace in red.
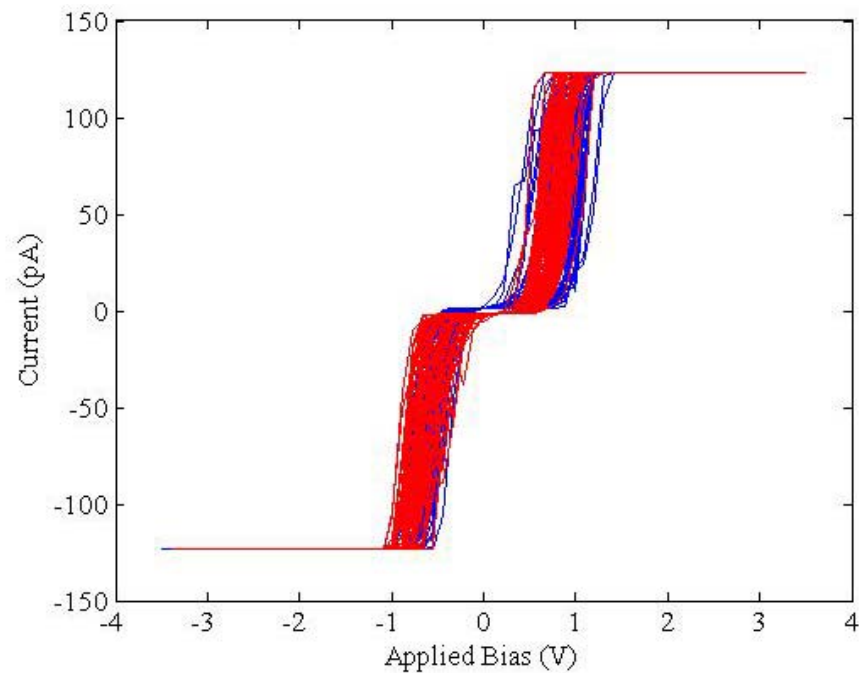

Figure 40. Tuna data for the 135 sec sample at 10pA/V current sensitivity for all 5 locations and 76 captures at each location. Trace data is shown in blue and retrace in red.

Figure 41. Tuna data for the 5 min sample at 10pA/V current sensitivity for all 5 locations and 76 captures at each location. Trace data is shown in blue and retrace in red.
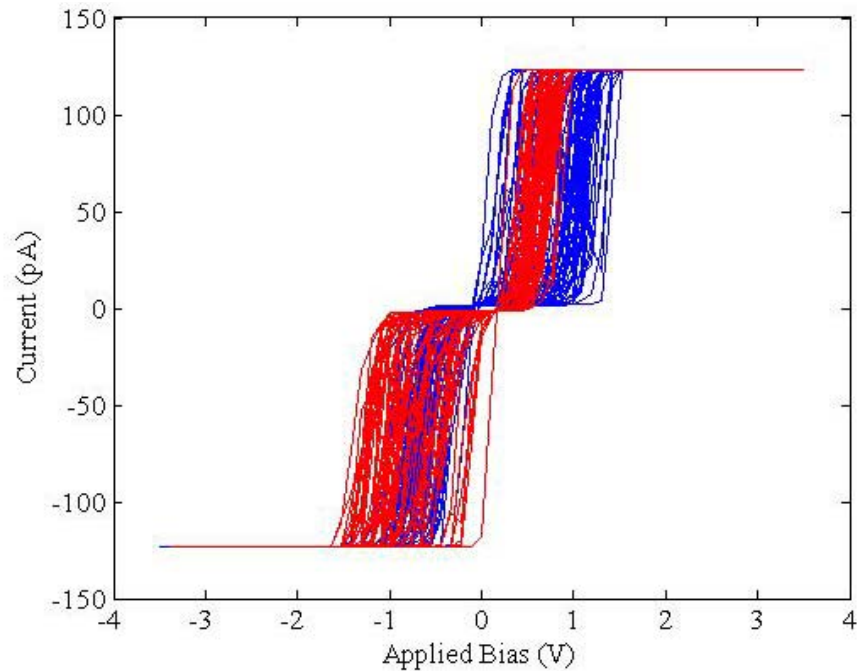

Figure 42. Tuna data for the 10 min sample at 10pA/V current sensitivity for all 5 locations and 76 captures at each location. Trace data is shown in blue and retrace in red.

Figure 43. Tuna data for the 30 min sample at 10pA/V current sensitivity for all 5 locations and 76 captures at each location. Trace data is shown in blue and retrace in red.
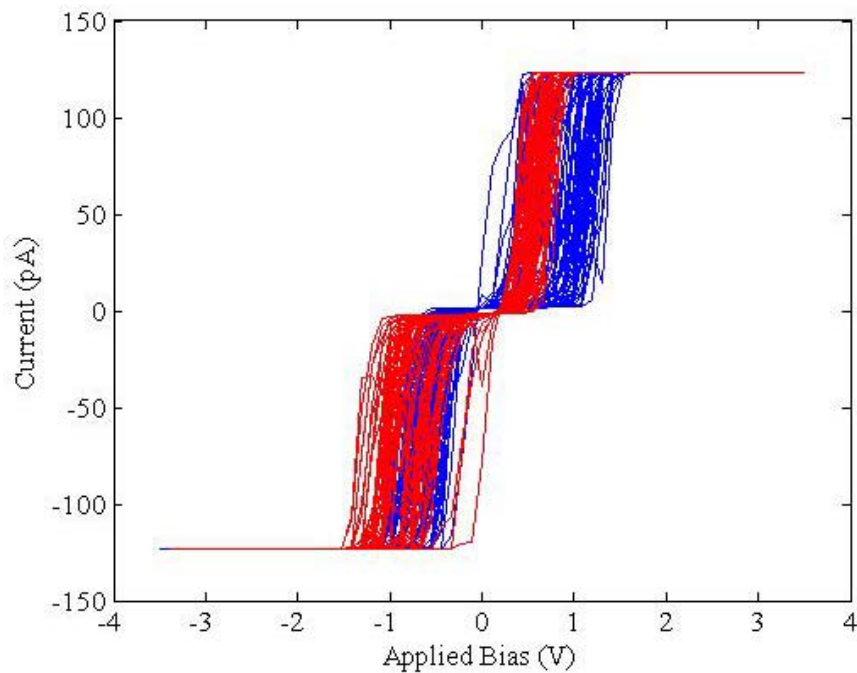

Figure 44. Tuna data for the 45 min sample at 10pA/V current sensitivity for all 5 locations and 76 captures at each location. Trace data is shown in blue and retrace in red.
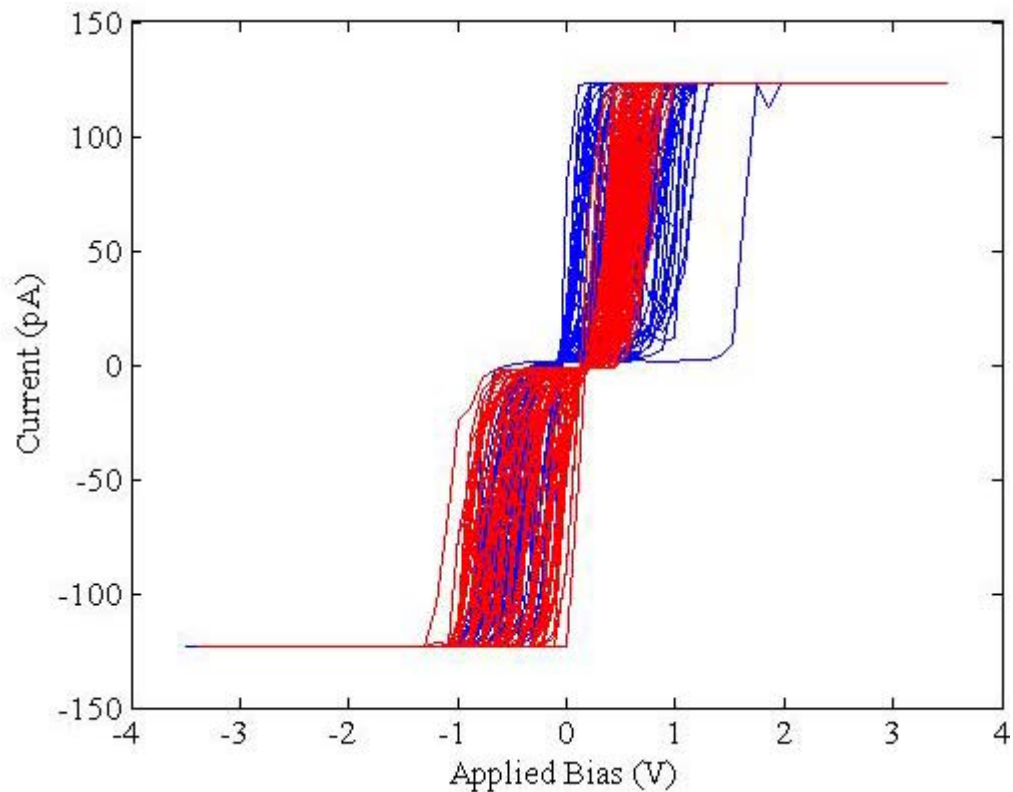
Figure 45. Tuna data for the 60 min sample at 10pA/V current sensitivity for all 5 locations and 76 captures at each location. Trace data is shown in blue and retrace in red.
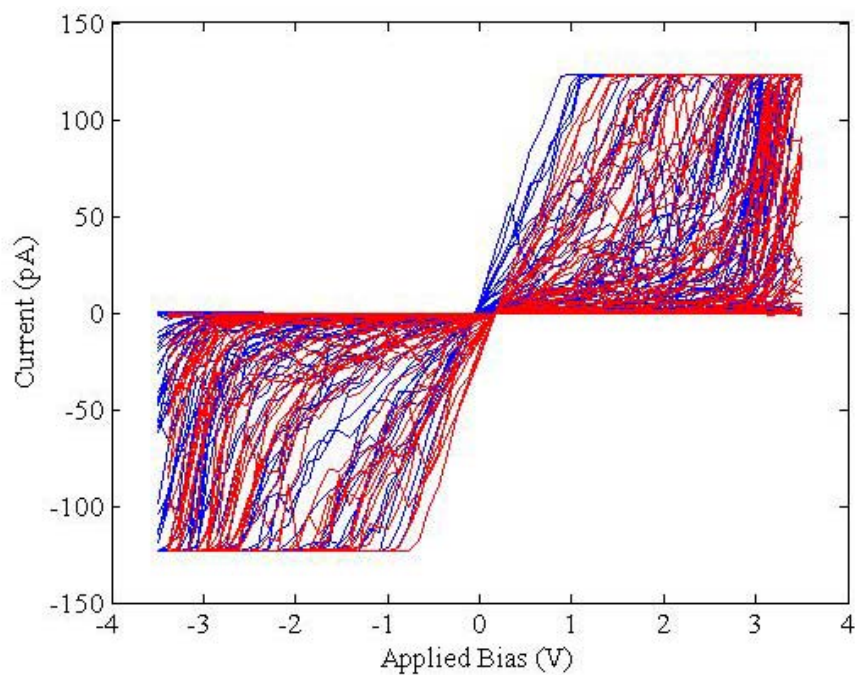

Figure 46. Tuna data for the 120 min sample at 10pA/V current sensitivity for all 5 locations and 76 captures at each location. Trace data is shown in blue and retrace in red.
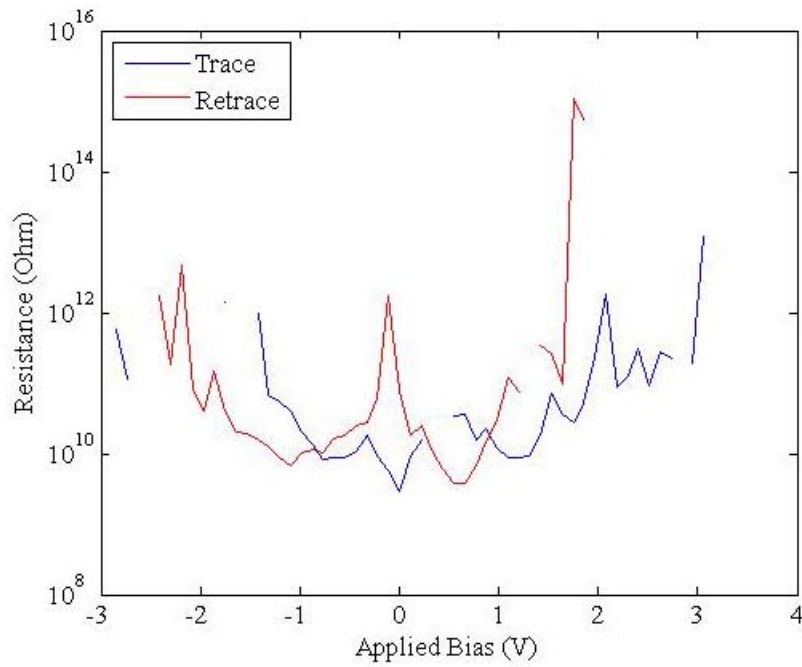
Appendix C.3 Resistance

Figure 47. Average resistance vs applied voltage for the base sample measured at 10pA/V current sensitivity.
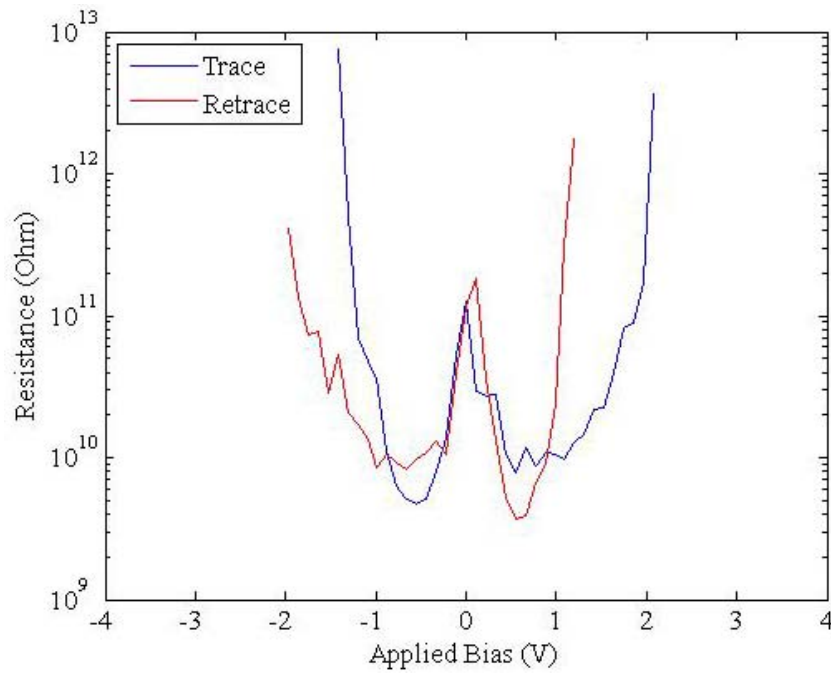

Figure 48. Average resistance vs applied voltage for the 45 second sample measured at 10pA/V current sensitivity.
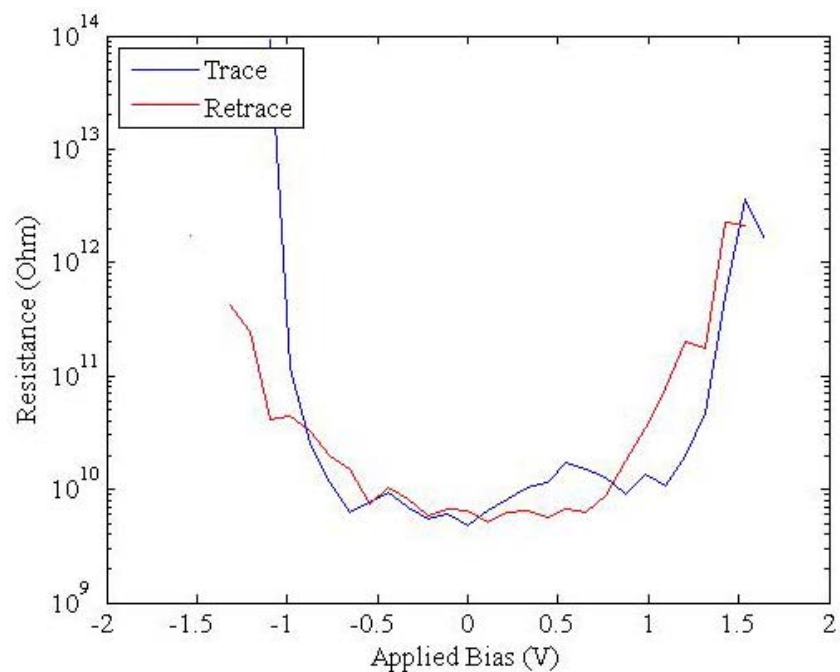
Figure 49. Average resistance vs applied voltage for the 90 second sample measured at 10pA/V current sensitivity.
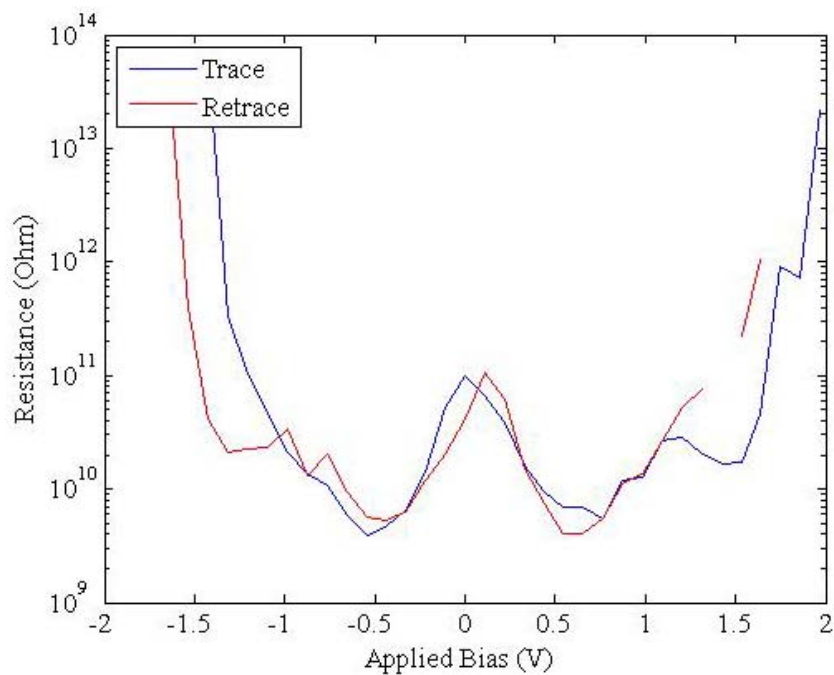

Figure 50. Average resistance vs applied voltage for the 135 second sample measured at 10pA/V current sensitivity.
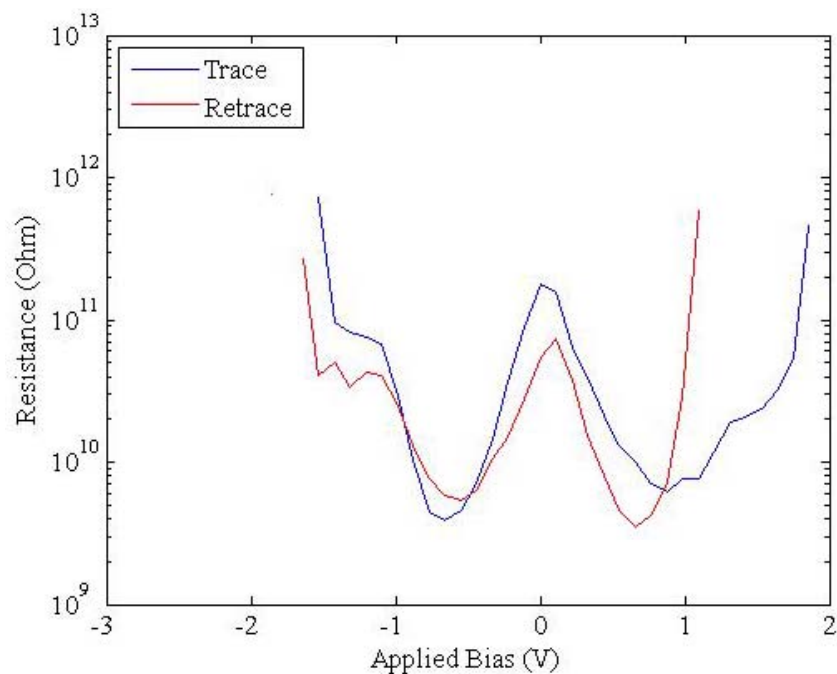
Figure 51. Average resistance vs applied voltage for the 5 minute sample measured at 10pA/V current sensitivity.

Figure 52. Average resistance vs applied voltage for the 10 minute sample measured at 10pA/V current sensitivity.

Figure 53. **Average resistance vs applied voltage for the 30 minute sample measured at 10pA/V current sensitivity.**

Figure 54. **Average resistance vs applied voltage for the 45 minute sample measured at 10pA/V current sensitivity.**
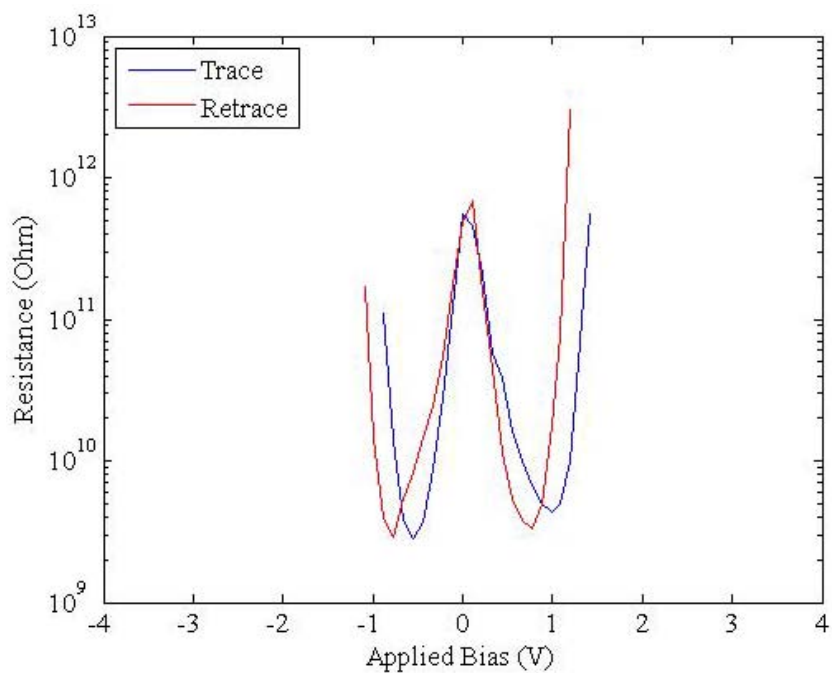
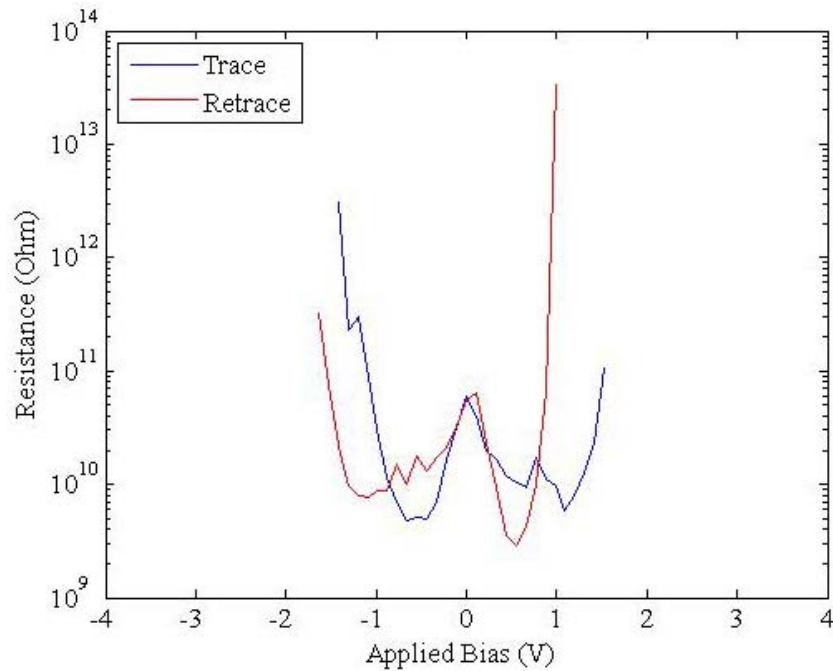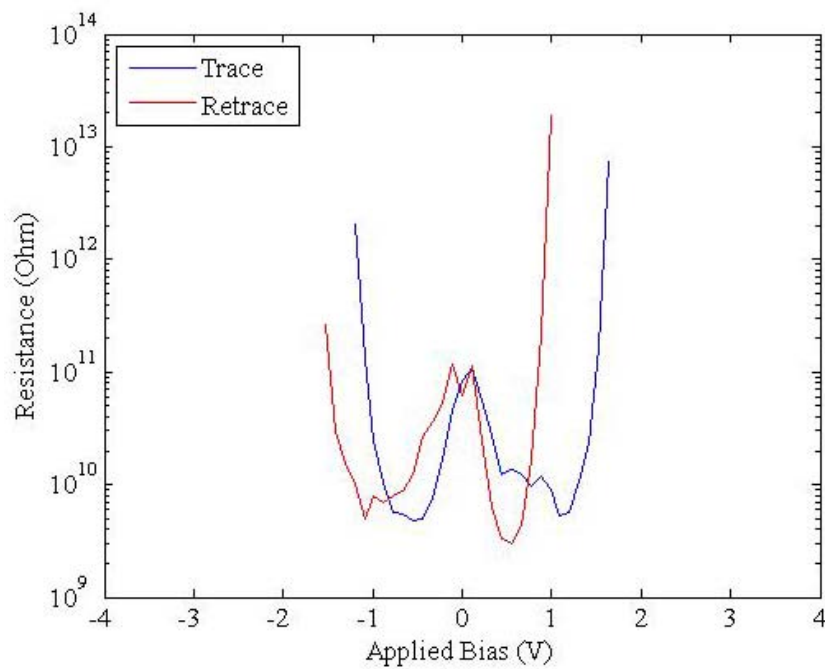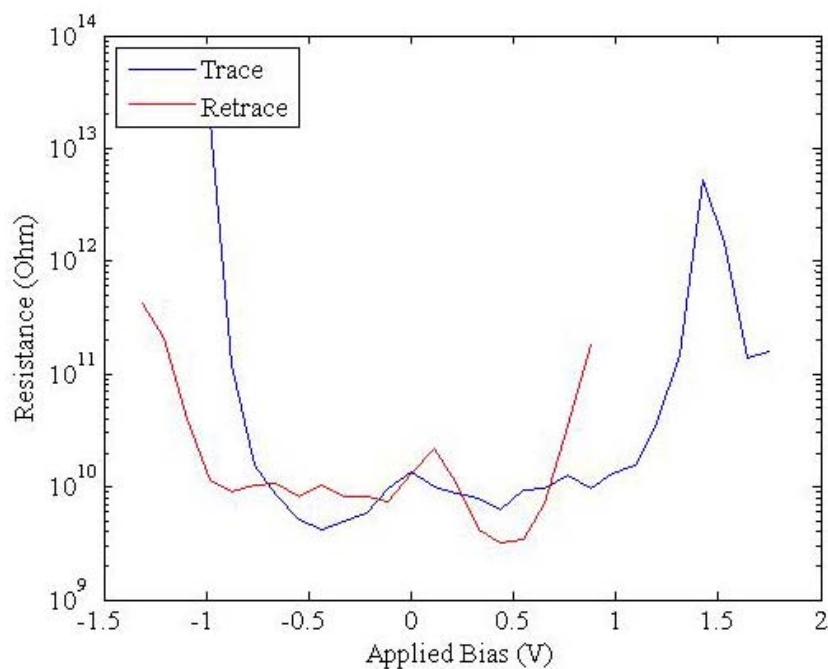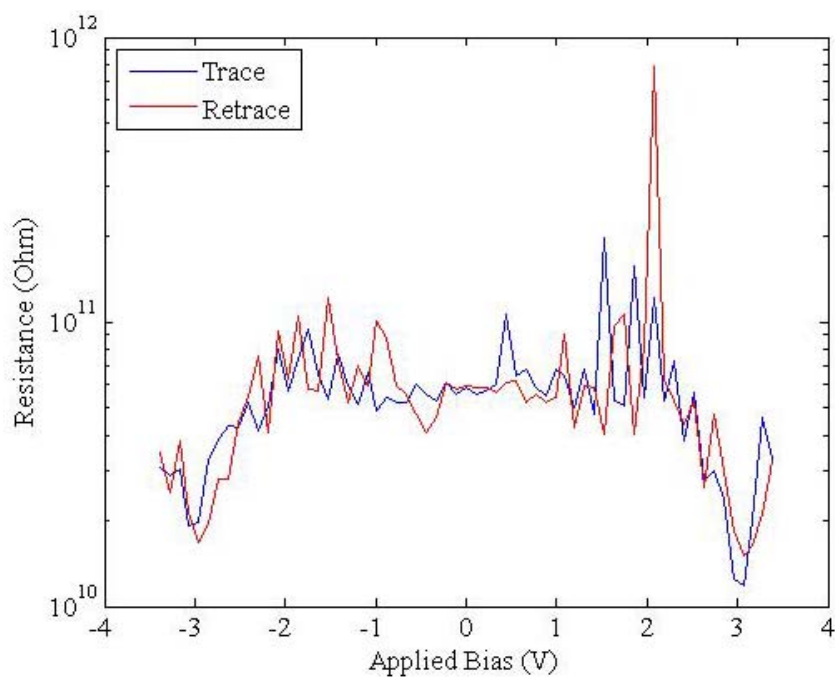**Figure 55. Average resistance vs applied voltage for the 60 minute sample measured at 10pA/V current sensitivity.**

Figure 56. Average resistance vs applied voltage for the 120 minute sample measured at 10pA/V current sensitivity.

71

Bibliography

[1] Rainer Waser, Regina Dittman, Georgi Staikov, and Kristof Szot, "Redox-Based Resistive Switching Memories–Nanoionic Mechanisms, Prospects, and Challenges," *Advanced Materials*, vol. 21, p. 2632–2663, 2009.

[2] Leon O Chua, "Memristor-The Missing Circuit Element," *IEEE Transactions on Circuit Theory*, vol. CT-18, no. 5, pp. 507-519, September 1971.

[3] Massimiliano Di Ventra, Yuriy V Pershin, and Leon O Chua, "Putting Memory Into Circuit Elements:Memristors, Memcapacitors, and Meminductors," *Proceedings of the IEEE*, vol. 97, pp. 1371-1372, August 2009.

[4] Dmitri B Strukov, Gregory S Snider, Duncan R Stewart, and R Stanley Williams, "The Missing Memristor Found," *Nature*, vol. 453, pp. 80-83, May 2008.

[5] D R Lamb and P C Rundle, "A non-filamentary switching action in thermally grown silicon dioxide films ," *British Journal of Applied Physics*, vol. 18, no. 1, p. 29, January 1967.

[6] F Argall, "Switching Phenomena in Titanium Oxide Thin Films," *Solid State Electronics*, vol. 11, pp. 535-541, 1968.

[7] R Yasuhara, Fujiwara, K Horiba, H Kumigashira, and M Kotsugi, "Inhomogeneous chemical states in resistance-switching devices with a planar-type Pt/CuO/Pt structure," *Applied Physics Letters*, vol. 95, p. 012110, 2009.

[8] R Stanley Williams. (2008, December) IEEE Spectrum. [Online]. http://spectrum.ieee.org/semiconductors/processors/how-we-found-the-missing-memristor/0

[9] Kohei Fujiwara, Takumi Nemoto, and Marcelo J Rozenberg, "Resistance Switching and Formation of a Conductive Bridge in Metal/Binary Oxide/Metal Structure for Memory Devices," *Japanese Journal of Applied Physics*, vol. 47, no. 8, p. 6266–6271, 2008.

[10] Murray A Lampert, "Simplified Theory of Space-Charge-Limited Currents in an Insulator with Traps," *Physical Review*, vol. 103, no. 6, pp. 1648-1656, September 1956.

[11] R Dong et al., "Reproducible hysteresis and resistive switching in metal-CuxO-metal," *Applied Physics Letters*, vol. 90, p. 042107, 2007.

[12] A E Rakhshani, "Thermostimulated impurity conduction in characterization of electrodeposited Cu2O films," *Journal of Applied Physics*, vol. 69, no. 4, pp. 2290-2295, February 1991.

[13] L Chaal et al., "Comparative AFM nanoscratching tests in air of bulk copper and electrogenerated cuprous oxide films," *Surface Science*, vol. 605, pp. 121-130, 2011.

[14] Klaus Schroder and Demir Onengut, "Optical Absorption of Copper and Copper-Rich Nickel Alloys at Room Temperature," *Physical Review*, vol. 162, no. 3, pp. 628-631, October 1967.

[15] A Parretta et al., "Electrical and Optical Properties of Copper Oxide Films Prepared by Reactive RF Magnetron Sputtering," *physica status solidi* , vol. 155, no. 2, pp. 399-404, June 1996.

[16] K Borgohain, N Murase, and S Mahamuni, "Synthesis and properties of Cu2O quantum particles," *Journal of Applied Physics*, vol. 92, no. 3, pp. 1292-1297, August 2002.

[17] Shigehito Deki, Kensuke Akamatsu, Tetsuya Yano, Minoru Mizuhata, and Akihiko Kajinami, "Preparation and characterization of copper(I) oxide nanoparticles dispersed in a polymer matrix," *Journal of Materials Chemistry*, vol. 8, p. 1865–1868, 1998.

[18] E Knözinger, A Kellersohn, W Langel, and M Giersig, "Cu2O quantum-dot particles prepared from nanostructured copper," *Advanced Materials*, vol. 7, p. 652–655, 1995.

[19] S Banerjee and D Chakravorty, "Optical absorption by nanoparticles of Cu2O," *Europhysics Letters*, vol. 52, no. 4, pp. 468-473, November 2000.

[20] Gunter Schmid, Ed., *Nanoparticles: from theory to application*. Germany: Wiley-VCH, 2004.

[21] Woo-Young Yang, Wan-Kee Kim, and Shi-Woo Rhee, "Radio frequency sputter deposition of single phase cuprous oxide using Cu2O as a target material and its resistive switching properties," *Thin Solid Films*, vol. 517, pp. 967-971, 2008.

[22] P Lauque, M Bendahan, J-L Seguin, M Pasquinelli, and P Knauth, "Electrical Properties of Thin-Films of the Mixed Ionic-electronic Conductor CuBr: Influence of Electrode Metals and Gaseous Ammonia," *Journal of the European Ceramic Society*, vol. 19, pp. 823-826, 1999.

[23] W Dieterich, P Fulde, and I Peschel, "Theoretical models for superionic conductors," *Advances in Physics*, vol. 29, no. 3, pp. 527-605, May 1980.

[24] A E Rahkshani, "Preparation, Characteristics and Photovoltaic Properties of Cuprous Oxide-A Review," *Solid-State Electronics*, vol. 29, no. 1, pp. 7-17, 1986.

[25] W Dieterich, "RECENT DEVELOPMENTS IN THE THEORY OF SOLID ELECTROLYTES," *Solid State Ionics*, vol. 40/41, pp. 509-515, 1990.

1. REPORT DATE (DD-MM-YYYY) 24-03-2011	2. REPORT TYPE Master's Thesis	3. DATES COVERED (From – To) Aug 2009 – March 2011

4. TITLE AND SUBTITLE Memristive Properties of Thin Film Cuprous Oxide	5a. CONTRACT NUMBER N/A
	5b. GRANT NUMBER N/A
	5c. PROGRAM ELEMENT NUMBER N/A
6. AUTHOR(S) Castle, Brett C., Capt, USAF	5d. PROJECT NUMBER N/A
	5e. TASK NUMBER N/A
	5f. WORK UNIT NUMBER N/A

7. PERFORMING ORGANIZATION NAMES(S) AND ADDRESS(S) Air Force Institute of Technology Graduate School of Engineering and Management (AFIT/EN) 2950 Hobson Way WPAFB OH 45433-7765	8. PERFORMING ORGANIZATION REPORT NUMBER AFIT/GMS/ENP/11-M01

9. SPONSORING/MONITORING AGENCY NAME(S) AND ADDRESS(ES) Air Force Research Laboratory/RITC (Dr. Joseph Van Nostrand) 525 Brooks Rd. Rome, NY 13441	10. SPONSOR/MONITOR'S ACRONYM(S) AFRL/RITC
	11. SPONSOR/MONITOR'S REPORT NUMBER(S) 1

12. DISTRIBUTION/AVAILABILITY STATEMENT APPROVED FOR PUBLIC RELEASE; DISTRIBUTION UNLIMITED.

13. SUPPLEMENTARY NOTES

14. ABSTRACT

Memristive properties of thin film copper oxides with different grain sizes were characterized using tunneling atomic force microscopy (TUNA) and optical reflection measurements. The thin films containing copper ions of different chemical states were prepared by thermal oxidation of metallic copper thin films, deposited via magnetron sputtering onto silicon wafer substrates at an elevated temperature for various lengths of time. The TUNA measurements showed a memristive hysteresis in the I-V curves under an applied bias profile with an initial bias of -3.5V, a ramp up to 3.5V, and subsequent return to -3.5V. Histogram analysis of the barrier height distribution for the forward and backward bias indicated that the barrier height fluctuates in a narrow range of bias voltages that are related to electrochemical potentials for oxidation/reduction of copper ions. Changes in chemical state of copper atoms were identified by optical reflectance measurements in UV-VIS-NIR wavelength regions. The growth of the thin films, including grain size, were characterized by topographic AFM imaging and changes in optical absorption bands due to the quantum size confinement effects. The fluctuations in the I-V measurements are theorized to be results of electrochemical changes as mobile ions migrate along grain boundaries due to heterogeneities in grain orientation/structure. A subtle periodic behavior and the variability of the I-V data suggest a correlation with grain size distribution. The asymmetric distribution in the barrier height may indicate that a different probability for injecting an electron in and withdrawing an electron from the films

15. SUBJECT TERMS **Cuprous oxide, memristor, thin film, TUNA, ionic conductor**

16. SECURITY CLASSIFICATION OF:			17. LIMITATION OF ABSTRACT	18. NUMBER OF PAGES	19a. NAME OF RESPONSIBLE PERSON **Dr. Alex Li, AFIT/ENP**
a. REPORT U	b. ABSTRACT U	c. THIS PAGE U	UU	85	19b. TELEPHONE NUMBER (Include area code) (937) 255-3636 x4576;alex.li@afit.edu